International Journal of Nanomedicine

Dovepress
Taylor & Francis Group

Open Access Full Text Article

ORIGINAL RESEARCH

CA9-Targeted Liposomal Delivery of siETS1 Inhibits Clear Cell Renal Cell Carcinoma Progression by Disrupting the ETS1/MYC Regulatory Axis

Yuyang Ye[1], Jing Sun[2], Yizheng Zhang[1], Shenghan Wang[3], Zhaoqian Meng[4]

[1]Department of Anesthesiology, The Second Qilu Hospital of ShanDong University, ShanDong University, Jinan, 250033, People's Republic of China; [2]Cheeloo College of Medicine, Shandong University, Jinan, 250012, People's Republic of China; [3]Shandong Provincial Hospital Affiliated to Shandong First Medical University, Shandong First Medical University, Jinan, 250021, People's Republic of China; [4]Affiliated Hospital of Shandong University of Traditional Chinese Medicine, Shandong University of Traditional Chinese Medicine, Jinan, 250011, People's Republic of China

Correspondence: Zhaoqian Meng, Affiliated Hospital of Shandong University of Traditional Chinese Medicine, Shandong University of Traditional Chinese Medicine, Jinan, 250011, People's Republic of China, Tel +86 13940442192, Email szymzq@163.com

Background: Clear cell renal cell carcinoma (ccRCC) is a highly aggressive malignancy with a high rate of recurrence and limited therapeutic options. Carbonic anhydrase IX (CA9) is characteristically overexpressed on the surface of ccRCC cells, making it a promising target for site-specific drug delivery. However, identifying the key molecular drivers of ccRCC progression and developing efficient, targeted nanomedicines remain critical challenges in current research.

Methods: Bioinformatics analysis of TCGA and single-cell RNA sequencing data was used to elucidate the ETS1/MYC axis. Direct transcriptional regulation of MYC by ETS1 was experimentally validated by chromatin immunoprecipitation-quantitative PCR (ChIP-PCR) and dual-luciferase reporter assays. An optimized CA9-targeting peptide, CaIX-P7, was designed via computational modeling and mutation screening, with affinity validated by surface plasmon resonance (SPR). siETS1-loaded liposomal nanoparticles (LNPs) were prepared using microfluidics and surface-functionalized with CaIX-P7 (ETS1@Lip-CAIX). The nanoparticles were characterized for size, zeta potential, and encapsulation efficiency. Therapeutic efficacy was evaluated in ccRCC cell lines (786-O, A-498), patient-derived organoids (PDO), and nude mouse xenograft models.

Results: Single-cell analysis identified ETS1 and MYC as synergistically activated transcription factors within tumor epithelial cells. Mechanistically, ChIP-PCR and dual-luciferase assays demonstrated that ETS1 promotes MYC transcription through this specific binding site, establishing ETS1 as a direct transcriptional activator of MYC. The optimized peptide CaIX-P7 demonstrated superior binding affinity to CA9 (Kd=52.96 nM) compared to its precursor. The engineered ETS1@Lip-CAIX nanoparticles exhibited a stable size of 154.8 nm and high siRNA encapsulation efficiency (89.1%). Systematic evaluation revealed that ETS1@Lip-CAIX effectively silenced the ETS1/MYC axis, leading to significant growth inhibition across all models, including patient-derived 3D organoids and in vivo xenografts, showed no discernible morphological alterations or pathological damage in major organs.

Conclusion: This study identifies the ETS1/MYC axis as a novel therapeutic target in ccRCC. We further successfully developed a CA9-targeted nanoplatform, ETS1@Lip-CAIX, which exhibits robust anti-tumor efficacy by disrupting this newly discovered regulatory hub. These findings provide a foundation for future translational studies of ccRCC.

Plain Language Summary: Clear cell renal cell carcinoma (ccRCC) is the most aggressive and common type of kidney cancer. Despite improvements in surgery and existing drugs, many patients face high recurrence rates and limited treatment options. Through advanced data analysis and laboratory experiments, we identified a critical growth engine in kidney cancer cells called the ETS1/MYC axis. This pathway acts as a switch that drives rapid tumor cell multiplication. Our study found that patients with high levels of these factors typically have a poorer prognosis. To shut down this growth engine, we engineered a smart delivery system called ETS1@Lip-CAIX. This system consists of tiny lipid-based carriers (nanoparticles) loaded with a genetic drug (siRNA) designed to silence the ETS1 gene. To ensure the drug reaches its target, we attached a specialized GPS peptide (CaIX-P7) to the surface. This peptide specifically recognizes and binds to CA9, a protein that is overexpressed on the surface of kidney cancer cells but rarely found in healthy kidneys. We tested this nanomedicine using diverse models, including traditional cell cultures, patient-derived 3D organoids (mini-tumors that mimic real patient biology), and animal models. Results demonstrated that the targeted nanoparticles significantly

https://doi.org/10.2147/IJN.S596277
Received: 6 February 2026
Accepted: 13 May 2026
Published: 22 May 2026

inhibited tumor growth by disrupting the ETS1/MYC axis. Crucially, the treatment showed no toxicity to normal cells, indicating high safety and biocompatibility. This research identifies a novel therapeutic target and presents a precise, highly effective nanomedicine strategy. It provides a promising new avenue for personalized treatment of aggressive kidney cancer, potentially improving survival rates while minimizing side effects for patients.

Keywords: ccRCC, ETS1, CA9, patient-derived organoids, liposomal nanoparticles, siRNA delivery

Graphical Abstract

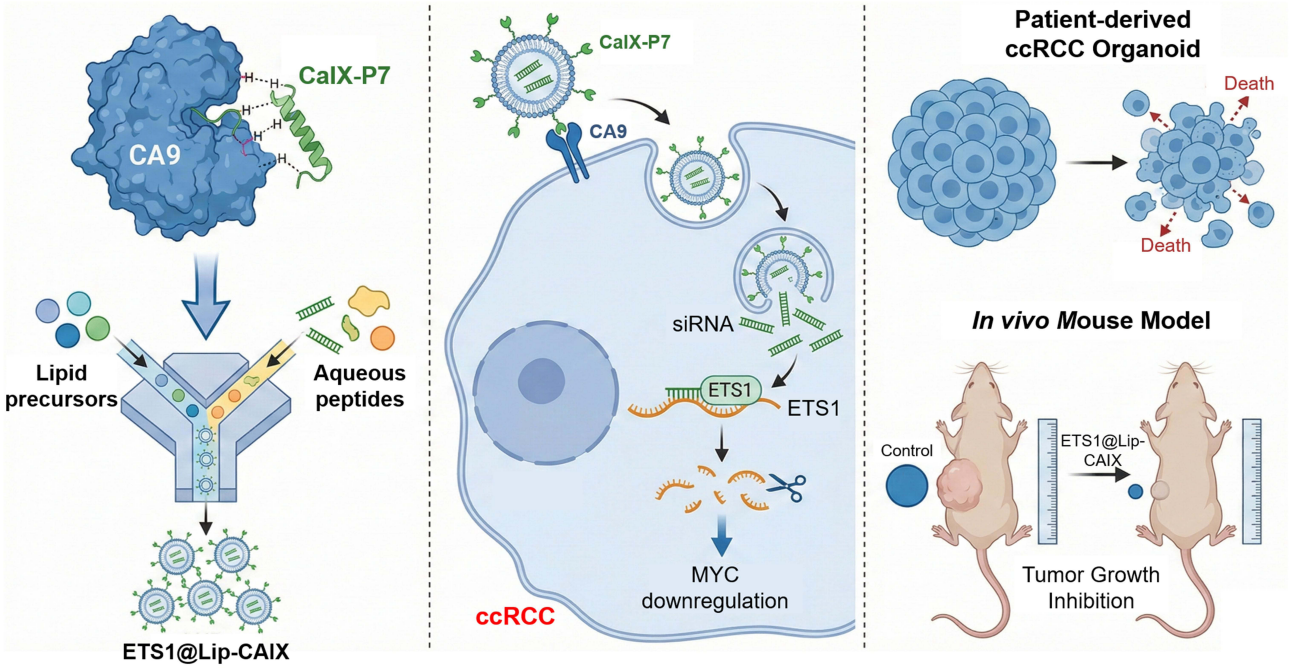

Introduction

Clear cell renal cell carcinoma (ccRCC) is a highly aggressive malignancy characterized by a high recurrence rate and limited therapeutic options. While advances have been made in surgical and systemic therapies, the prognosis for patients with advanced ccRCC remains unsatisfactory.[1,2] Carbonic anhydrase IX (CA9) is characteristically overexpressed on the surface of ccRCC cells, making it a promising target for site-specific drug delivery.[3,4] However, identifying the key molecular drivers of ccRCC progression and developing efficient, targeted nanomedicines remain critical challenges in current research.

ETS1, a key member of the ETS transcription factor family, plays a significant role in the evolution of various malignancies.[5,6] Studies have shown that ETS1 expression is remarkably higher in ccRCC tissues.[7] Although previous studies suggest that ETS1 possesses oncogenic potential, the specific molecular regulatory mechanisms and downstream signaling pathways of ETS1 in ccRCC progression require further in-depth investigation. Elucidating these mechanisms is essential for developing novel therapeutic interventions for ccRCC.

To achieve precise delivery of therapeutic agents to ccRCC tissues, lipid nanoparticles (LNPs) have gained significant attention due to their excellent biocompatibility and high nucleic acid encapsulation capacity.[8–10] Nevertheless, the targeting efficiency of traditional nanocarriers is often restricted. Optimized targeting peptides can significantly enhance the targeting capability of nanoparticles toward tumor cells. Utilizing such advanced targeting strategies to deliver small interfering RNA (siRNA) to silence critical oncogenes provides a new direction for the molecularly targeted therapy of ccRCC.[11,12]

This study aims to develop a novel CA9-targeted lipid nanoparticle system for the precise delivery of siETS1 to interfere with the progression of ccRCC. In this study, through the analysis of single-cell RNA sequencing data, bioinformatics, and clinical patient samples, we have revealed a novel molecular axis regulated by ETS1. We designed and validated an optimized targeting peptide, CaIX-P7, which exhibits exceptionally high affinity and significantly improves the delivery efficiency of the nanoparticles. Furthermore, we systematically evaluated the therapeutic efficacy of this nanoplatform using patient-derived organoids (PDO) and multiple xenograft models. This research not only identifies a potential therapeutic target for ccRCC but also demonstrates a precise nanomedicine strategy with promising clinical translational potential for the treatment of aggressive kidney cancer.

Materials and Methods

Data Acquisition and Processing

Single-cell RNA-seq data for GSE178481 (comprising 26 samples from ccRCC patients, including treatment-naive primary tumors and matched adjacent normal tissues) were obtained from the GEO database. Gene-by-cell count matrices were imported into Seurat (v4.3.0) for downstream analysis.

Quality control and filtering: Cells were filtered based on the following criteria: (1) gene counts between 200 and 8,000; (2) unique molecular identifier (UMI) counts between 500 and 50,000; (3) mitochondrial gene percentage<15%; and (4) hemoglobin gene percentage<5%. Before quality control, the dataset contained 87,432 cells. After applying these filtering thresholds, 72,156 cells (82.5%) were retained for downstream analysis.

Normalization, integration, and batch effect correction: Library-size normalization was performed using the Normalize Data function with a scale factor of 10,000. The top 2,000 highly variable genes were identified using the Find Variable Features function with the vst selection method. Batch correction was performed using the Harmony algorithm (v1.0) with the sample identity as the batch variable. Principal component analysis (PCA) was conducted on the integrated data, and the top 30 principal components were selected for downstream dimensionality reduction and clustering based on the elbow plot.

Clustering and annotation: Unsupervised clustering was performed using the Find Neighbors function on the first 30 PCs, followed by FindClusters with a clustering resolution of 0.8. UMAP embeddings were used for visualization. Cell type annotation was performed using a multi-modal approach combining canonical marker gene expression, Single R (v2.0) automated annotation with the Human Primary Cell Atlas as reference, and manual curation based on established literature markers. Major cell populations were identified as follows: tumor epithelial cells ($CA9^+$, $KRT8^+$, $KRT18^+$), normal epithelial cells ($PAX2^+$, $PAX8^+$, $CA9^-$), fibroblasts ($COL1A1^+$, $ACTA2^+$), myeloid cells ($CD14^+$, $CD68^+$, $CD163^+$), NK cells ($NKG7^+$, $GNLY^+$), T cells ($CD3D^+$, $CD3E^+$), B cells ($CD79A^+$, $MS4A1^+$), and endothelial cells ($PECAM1^+$, VWF^+). Malignant epithelial cells were distinguished from non-tumor epithelial cells using a combination of copy number variation (CNV) inference via inferCNV (v1.14.0) with normal epithelial cells as the reference, elevated CA9 expression (> 2-fold compared to normal epithelial mean), and co-expression of established ccRCC tumor markers (NDUFA4L2, VEGFA, and SLC6A3). Cells classified as CNV-high with concurrent CA9 upregulation were designated as tumor epithelial cells.

A shared nearest neighbor graph was constructed in PCA space and cells were clustered using a graph-based method. UMAP embeddings were used for visualization. Expression of selected genes (ETS1 and MYC) was visualized on UMAP and summarized across clusters using standard Seurat plots.

To identify key molecular drivers in ccRCC tumor clusters, we performed integrated gene regulatory network analysis using two complementary approaches on the tumor epithelial cells subset. Co-expression modules were identified via GRNBoost2 implemented in pySCENIC (v0.12.1) on tumor epithelial cells. DNA-motif enrichment analysis was performed using RcisTarget with the hg19-500bp-upstream-7species database (motif ranking threshold < 500, NES > 3.0) to retain only direct TF targets, yielding regulons whose activities were quantified using AUCell with automatic threshold estimation. Regulon specificity scores were calculated using Jensen-Shannon divergence to identify cluster-specific TFs. Independently, TF protein activity was inferred on the identical malignant cell subset using the VIPER framework implemented in decoupleR (v2.4.0), leveraging DoRothEA human regulons as the prior TF-target network.

TFs ranking in the top 10 (Supplementary Table S1) by both pySCENIC regulon specificity scores and VIPER normalized enrichment scores (NES > 3.0) were selected as core drivers.

To visualize the ETS1/MYC regulatory module, a protein-protein interaction network was constructed using the STRING database (v12.0, https://string-db.org). The input query consisted of ETS1 and MYC as core TFs, supplemented by their first-order interacting partners retrieved from STRING with confidence scores > 0.700 based on experimental evidence and database curation. This yielded a high-confidence network comprising 8 nodes (ETS1, MYC, MAX, DAXX, SP100, PIM1, PIM2, and USP28) and 14 edges (network density = 0.500, clustering coefficient = 0.786). Interaction parameters were set as follows: organism Homo sapiens, confidence score > 0.700 (high confidence).

Based on the network inference, we hypothesized that ETS1 directly regulates MYC transcription. Putative ETS1 binding sites within the human MYC promoter region (−2000 bp relative to the transcription start site) were predicted using JASPAR 2024 (matrix ID: MA0098.3, relative score > 0.8). The top-scoring binding site (P4: −1518 to −1513 bp, sequence 5'-CGGAAG-3') was experimentally validated by chromatin immunoprecipitation-quantitative PCR (ChIP-PCR) and dual-luciferase reporter assays.

For the prognostic analysis of ETS1 in ccRCC, RNA-seq data and corresponding clinical metadata were retrieved from TCGA-KIRC. ETS1 expression was stratified into high and low groups using the optimal cut-off value determined by the maximally selected rank statistics via the surv_cutpoint function from the survminer R package (v0.4.9), which identified an optimal cut-off of 9.82 log2(TPM+1). Kaplan-Meier survival curves were generated, and statistical significance was assessed using the Log rank test. Univariable Cox proportional hazards regression analysis yielded a hazard ratio (HR) of 2.34 (95% CI: 1.42–3.86; P = 0.00063) for high ETS1 expression. Additionally, a multivariable Cox regression model was constructed adjusting for age, gender, tumor stage, and Fuhrman grade, which confirmed ETS1 as an independent prognostic predictor (adjusted HR = 2.01, 95% CI: 1.18–3.42; P = 0.0098). All survival analyses were performed using the survival (v3.5–5) and survminer (v0.4.9) R packages.

Preparation of ETS1@Lip and ETS1@Lip-CAIX

LNPs were prepared using a microfluidic mixing technique. Briefly, the ionizable lipid DLin-MC3-DMA, DSPC, cholesterol, and PEG-lipids (DSPE-PEG2000 and DSPE-PEG2000-Maleimide) were dissolved in anhydrous ethanol at a molar ratio of 50:10:38:1.5:0.5. For siRNA-loaded LNPs, siRNA was dissolved in 50 mM citrate buffer (pH 4.0) to achieve a nitrogen-to-phosphate (N/P) ratio of 6:1. The aqueous and organic phases were mixed using a microfluidic chip mixer at a flow rate ratio of 3:1 (v/v) and a total flow rate of 12 mL/min. Blank LNPs were synthesized following the same procedure without the addition of siRNA. The resulting LNP solutions were dialyzed against phosphate-buffered saline (PBS, pH 7.4) for 24 h using a 100 kDa MWCO membrane to remove ethanol and neutralize the pH.

The targeting peptide CaIX-P7 (WNTNHVPLSPRY) was conjugated to the surface of LNPs via thiol-maleimide Michael addition chemistry. A cysteine residue was added to the N-terminus of the peptide sequence (Cys-WNTNHVPLSPRY). The peptide was then added to the siRNA-LNP suspension at a peptide-to-maleimide molar ratio of 2:1. The mixture was stirred at 4 °C for 12 h in the dark. Unreacted peptides were removed using centrifugal ultrafiltration (100 kDa MWCO). The final product was designated as ETS1@Lip-CAIX.

The hydrodynamic diameter, polydispersity index (PDI), and zeta potential of the three types of LNPs (CTRL LNPs, ETS1@Lip and ETS1@Lip-CAIX) were measured by dynamic light scattering (DLS) using a Zetasizer. The encapsulation efficiency (EE) of siETS1 was quantified using the Quant-it™ RiboGreen™ RNA Assay. In brief, LNPs were diluted in TE buffer in the presence or absence of 0.5% (v/v) Triton X-100 to determine the concentration of total and unencapsulated (free) siRNA, respectively. RiboGreen reagent was added to each sample. The EE was calculated according to the following equation: $EE\ (\%) = (siRNA_{Total} - siRNA_{Free})/siRNA_{Total} \times 100\%$. All characterization data were obtained from three independent batches.

Computational Design and Optimization of CA9-Targeting Peptides

The crystal structure of the human CA9 extracellular domain was retrieved from the Protein Data Bank (PDB ID: 5FL4, resolution 2.0 Å) and prepared as the receptor. Structure preparation included removal of crystallographic waters, addition of hydrogen atoms, and assignment of protonation states at pH 7.4 using the PDB2PQR server (v2.1.1) with

the AMBER force field. The 3D structures of the precursor peptide CaIX-P1 (YNTNHVPLSPKY) were predicted using the PEP-FOLD3 server, with the top five models selected based on their sOPEP energy scores for further analysis.[13] Protein-peptide docking was subsequently performed using the HADDOCK 2.4 web server. To guide the docking process, residues Y1, H5, V6, P7, L8, and Y12 of the peptide were designated as active residues based on alanine scanning data from the original phage display study and structure-activity relationship analysis: Y1 and Y12 mediate hydrophobic interactions with the CA9 catalytic cleft; H5 coordinates with the zinc-bound water molecule; and V6, P7, and L8 constitute the core hydrophobic binding interface. Passive residues were automatically defined within a 6.5 Å radius of active residues. The resulting docked complexes were ranked by HADDOCK scores and cluster sizes, and the top-scoring complex was selected for interface analysis. The binding interface was characterized using the PDBePISA server, including analysis of solvation free energy gain (ΔG_solv), hydrogen bond networks, and interface residue contacts. To enhance binding affinity, systematic mutation screening was conducted using the mCSM-PPI2 server. Single-point mutations were introduced across the CaIX-P1 sequence, and their impact on binding was quantified by predicting the change in binding free energy (ΔΔG = ΔG_mutant − ΔG_wild-type). Mutations with a predicted ΔΔG < −0.5 kcal/mol, indicating a predicted >2-fold affinity enhancement, were prioritized. Candidates were further filtered to exclude mutations disrupting peptide secondary structure (PEP-FOLD3 confidence score < 0.7) or introducing steric clashes (>0.4 Å van der Waals overlap). The remaining candidates were re-scored using HADDOCK, and the optimal mutant CaIX-P7 (WNTNHVPLSPRY), exhibiting a predicted ΔΔG of −1.24 kcal/mol was selected for experimental validation through SPR and cellular uptake assays.

Cell Culture

786-O and A-498 human ccRCC cell lines were purchased from the American Type Culture Collection (ATCC) (Catalog number: CRL-1932 and HTB-44, respectively). UCL-93, a human renal tubular epithelial cell line used as the normal control, was purchased from BeNa Culture Collection (BNCC, China) (Catalog number: BNCC342369). Cells were maintained in high-glucose DMEM supplemented with 10% fetal bovine serum at 37 °C in a humidified atmosphere containing 5% CO_2. Cells were treated with ETS1@Lip or ETS1@Lip-CAIX at a final siRNA concentration of 50 nM. For mRNA quantification (RT-PCR), cells were harvested 24 h post-treatment. For protein expression analysis (Western blot), cells were collected 48 h post-treatment. All cell lines were routinely tested for mycoplasma contamination using PCR-based detection methods, and no mycoplasma contamination was detected throughout the study period.

Cell Transfection

Transfections were performed in 6-well plates. Cells at 60–80% confluence were transfected with ETS1 siRNA using the Lipofectamine 3000 reagent (L3000015, Invitrogen, NY, USA). After transfection, cells were cultured for an additional 24–72 h before downstream assays. All transfections were carried out in triplicate. The sequences siETS1 (GenePharma, Shanghai, China) were shown in Table S2.

Cell Growth Assay by MTT

Cell proliferation was evaluated with the MTT assay. Cells were seeded in 96-well plates and subjected to the indicated treatments. At the designated time-points, 0.5 mg/mL MTT was added to each well and incubated for 4 h. The formazan crystals were dissolved in DMSO for 30 min, and absorbance was measured at 490 nm with a microplate reader.

Real-Time Quantitative PCR (RT-qPCR)

Total RNA was extracted with TRIzol when cells reached 85–95% confluence or at the end of the treatment period. RNA was reverse-transcribed using the MonScript™ RT III All-in-One Mix with dsDNase kit. The resulting cDNA was subjected to qPCR under the following conditions: 50 °C for 15 min, 95 °C for 5 min, followed by 35 cycles of 95 °C for 15s, 60 °C for 30s, and 72 °C for 1 min. Gene expression was normalized to GAPDH. The primer sequences were shown in Table S3.

Western Blot

Protein expression was examined by Western blot. Cells were lysed with RIPA buffer containing protease and phosphatase inhibitors. Equal amounts of protein were separated by SDS-PAGE and transferred onto PVDF membranes. Then incubated overnight at 4 °C with the following primary antibodies: GAPDH (2118, CST, MA, USA), ETS1 (14069, CST, MA, USA) and MYC (9402, CST, MA, USA). After three washes with TBST, membranes were incubated with the corresponding HRP-conjugated secondary antibody for 1 h at room temperature. Band density analysis was performed using Image J.

ChIP-PCR

786-O cells were cultured to 80–90% confluence and crosslinked with 1% formaldehyde at room temperature for 10 min to covalently link proteins to DNA. Crosslinking was quenched by adding glycine to a final concentration of 125 mM. Cells were collected, washed twice with ice-cold PBS, and resuspended in lysis buffer (1% SDS, 10 mM EDTA, 50 mM Tris-HCl, pH 8.1, supplemented with protease inhibitor cocktail) for 10 min on ice. Chromatin was sheared to 200–500 bp fragments using a Bioruptor sonicator (medium power, 30s ON/30s OFF, 15 cycles). After centrifugation at 12,000 × g for 10 min at 4°C, the supernatant was diluted 10-fold with ChIP dilution buffer (0.01% SDS, 1.1% Triton X-100, 1.2 mM EDTA, 16.7 mM Tris-HCl, pH 8.1, 167 mM NaCl). One percent of the diluted chromatin was reserved as Input control; the remainder was divided into two equal aliquots and incubated overnight at 4°C with rotation with either 5 μg anti-ETS1 antibody (14069, CST, MA, USA) or isotype-matched IgG (2729, CST, MA, USA). The following day, 30 μL Protein A/G magnetic beads (Thermo Fisher Scientific) were added and incubated for 2 h at 4°C with rotation to capture immune complexes. Beads were sequentially washed twice with low-salt wash buffer (0.1% SDS, 1% Triton X-100, 2 mM EDTA, 20 mM Tris-HCl, pH 8.1, 150 mM NaCl), high-salt wash buffer (same as low-salt but with 500 mM NaCl), LiCl wash buffer (0.25 M LiCl, 1% NP-40, 1% sodium deoxycholate, 1 mM EDTA, 10 mM Tris-HCl, pH 8.1), and TE buffer (10 mM Tris-HCl, 1 mM EDTA, pH 8.0). Immune complexes were eluted twice with 200 μL elution buffer (1% SDS, 0.1 M $NaHCO_3$) for 15 min each at room temperature with agitation. NaCl was added to both Input and eluted samples to a final concentration of 200 mM, followed by overnight reverse crosslinking at 65°C. Samples were then treated with proteinase K (20 μg/mL) at 45°C for 1 h, and DNA was purified by phenol-chloroform extraction and ethanol precipitation.

SYBR Green qPCR was performed to assess ETS1 enrichment at the predicted binding sites within the MYC promoter. Based on JASPAR predictions, three high-scoring sites were selected for validation: P1 (−146 to −141 bp), P2 (−656 to −651 bp), and P4 (−1518 to −1513 bp); primer P3 served as a negative control region. Primer sequences are listed in Table S3. Each 20 μL PCR reaction contained 10 μL 2× SYBR Green Master Mix, 0.4 μL of each primer (10 μM), 2 μL ChIP DNA template, and 7.2 μL nuclease-free water. Thermal cycling conditions were: 95°C for 3 min; 40 cycles of 95°C for 15s, 60°C for 30s, and 72°C for 30s. All samples were run in triplicate. Enrichment was calculated using the % IgG method: Ct values were first normalized to Input using the formula Ct_adjusted = Ct_ChIP − [Ct_Input − $\log_2$(Input dilution factor)]; the fold enrichment relative to IgG was then calculated as $2^{(-\Delta Ct)}$, where ΔCt = Ct_anti-ETS1_adjusted − Ct_IgG_adjusted.

Dual-Luciferase Reporter Assay

To validate the predicted ETS1 binding site, wild-type (WT) and mutant (Mut) MYC promoter luciferase reporter constructs were generated. For the WT construct, a 2 kb fragment of the human MYC promoter spanning from −2000 bp to the transcription start site (encompassing the P4 site) was amplified from human genomic DNA by PCR. KpnI and HindIII restriction sites were incorporated at the 5′ and 3′ ends of the primers, respectively, to facilitate directional cloning into the pGL3-Basic vector (Promega) upstream of the firefly luciferase gene. The Mut construct was generated by overlap extension PCR, in which the core P4 sequence (5′-CGGAAG-3′) was mutated to 5′-TTTTTT-3′ while preserving all flanking sequences. All constructs were verified by Sanger sequencing.

Twenty-four hours prior to transfection, 786-O cells were seeded into 24-well plates at a density of 1×10^5 cells per well. Each well was co-transfected with 200 ng of reporter plasmid (WT or Mut), 50 ng of pRL-TK Renilla luciferase internal

control plasmid (Promega), and either the ETS1 overexpression plasmid (pcDNA3.1-ETS1), using Lipofectamine 3000 (L3000015, Invitrogen) according to the manufacturer's protocol. The transfection medium was replaced with complete growth medium 6 h post-transfection. After 48 h, culture medium was aspirated and cells were gently washed twice with ice-cold PBS. Cells were lysed by adding 100 μL of 1× Passive Lysis Buffer (Promega) per well and rocking at room temperature for 15 min. Lysates were collected and clarified by centrifugation at 12,000 × g for 5 min.

For luminescence measurement, 20 μL of cleared lysate was transferred to a white 96-well plate and assayed on a GloMax Navigator Microplate Luminometer (Promega). Firefly luciferase activity was measured first by adding 50 μL of Luciferase Assay Reagent II (LAR II), mixing, and integrating photon counts for 10s after a 2s delay. Stop & Glo® Reagent (50 μL) was then added to quench firefly signal and initiate Renilla luciferase measurement, with photon counts integrated for 10s after a 2s delay. Each transfection group consisted of six biological replicates. Relative luciferase activity was normalized to Renilla luciferase activity to control for transfection efficiency and calculated as: relative activity = (firefly luciferase activity / Renilla luciferase activity) × 100%.

Surface Plasmon Resonance (SPR) Analysis

The binding affinities of the precursor peptide CaIX-P1 and the optimized peptides toward the recombinant human CA9 protein were quantitatively evaluated using SPR. The experiments were conducted on a Biacore system (Cytiva, MA, USA) at 25 °C. Briefly, the recombinant CA9 protein was immobilized onto the surface of a CM5 sensor chip using standard amine coupling chemistry. To determine the kinetic parameters, the peptides were dissolved in HBS-EP+ running buffer and prepared in a series of concentrations (ranging from 0 to 1,000 nM). Each concentration was injected over the sensor surface at a constant flow rate to monitor the association and dissociation phases. Between each cycle, the chip surface was regenerated with 10 mM glycine-HCl (pH 2.0) to remove any residual bound peptides. The obtained sensorgrams were processed and fitted to a 1:1 steady-state affinity model using Biacore evaluation software to calculate the equilibrium dissociation constant (Kd).

Patient-Sample Collection and Organoid Culture

Fresh ccRCC tumor specimens were obtained immediately after nephrectomy from 30 consecutive patients who met the inclusion criteria (histologically confirmed clear cell renal cell carcinoma, no prior systemic therapy, and age ≥18 years) between May 1, 2024, and September 1, 2025. The cohort comprised 19 male and 11 female patients with a mean age of 58.4 ± 9.7 years (range: 42–76 years). According to the TNM classification, 8 patients were stage I, 12 were stage II, 7 were stage III, and 3 were stage IV. Fuhrman grade distribution was as follows: grade 1 (n=4), grade 2 (n=11), grade 3 (n=10), and grade 4 (n=5). Of the 30 collected samples, 18 successfully developed into stable organoid lines (success rate: 60%), while 12 samples failed to establish due to insufficient viable cell yield (n=7) or bacterial contamination during initial culture (n=5). Among the 18 established PDO lines, two representative lines (PDO #1 and PDO #2) were selected for subsequent therapeutic evaluation based on their robust growth characteristics and stable passage capability (>10 passages). Tissue fragments were minced and digested with collagenase IV (1 mg/mL) for 30 min at 37 °C with intermittent pipetting to ensure complete dissociation. The cell suspension was filtered through a 70-μm strainer, washed twice with cold PBS, and embedded in Growth Factor Reduced Matrigel (356231, Corning). Domes were overlaid with complete ccRCC organoid medium (K2171-KC, Bozhengyuan Biotech, China) and cultured at 37 °C in 5% CO_2; medium was replenished every 3–4 days. The study involving human clinical samples was approved by the Ethics Committee of the Second Hospital of Shandong University (Approval No. KYLL2025605) prior to the initiation of patient recruitment and sample collection, and written informed consent was obtained from all participating patients. All procedures performed in this study involving human participants were in accordance with the ethical standards of the institutional research committee and with the Declaration of Helsinki.

Murine Xenograft Assay

To evaluate the therapeutic potential of the targeted nanoparticles, three independent subcutaneous xenograft models were established using 786-O cells, A-498 cells, and patient-derived ccRCC organoid (PDO). The sample size was determined a priori based on power analysis using GPower 3.1 software. Based on our pilot experiments (n = 3 per

group), the expected effect size for tumor volume reduction in the ETS1@Lip-CAIX group compared to the control group was Cohen's d = 2.8 (large effect). With an alpha level of 0.05 (two-tailed), a power (1-β) of 0.90, and assuming a one-way ANOVA design with 3 groups, the minimum required sample size was calculated as n = 4 per group. To account for potential attrition (estimated at <10%) and to ensure robust statistical power for subgroup comparisons, we enrolled n = 5 mice per group (total n = 15 per model; 45 mice overall). This sample size provides >95% power to detect the anticipated effect size, exceeding the conventional 80% threshold for animal studies. For cell line-derived models, 1×10^7 cells (in a 1:1 mixture of PBS and Matrigel) were injected subcutaneously into the right flank of 6-week-old female athymic nude mice. For the PDO-derived model, stable 3D organoid fragments were similarly inoculated into the flank. When the average tumor volume reached approximately 100 mm^3, mice from each model (n = 45 in total, n = 15 per model) were randomized into three treatment groups (n = 5 per group) using a computer-generated random number sequence: (1) Saline (CTRL), (2) non-targeted ETS1@Lip, and (3) targeted ETS1@Lip-CAIX. Nanoparticles were administered via tail vein injection at a dose of 1.5 mg siRNA/kg body weight. Treatments were performed every 3 days for a total of 8 doses over the 24-day experimental period. Tumor length (L) and width (W) were measured using digital calipers every 3 days, and tumor volume (V) was calculated using the formula $V= 1/2 \times L \times W^2$. Animal body weight and behavioral signs of toxicity were monitored daily. Mice were humanely euthanized on Day 24 via cervical dislocation under deep anesthesia (3% isoflurane). Tumors were excised, photographed, and weighed. Excised tissues were either snap-frozen in liquid nitrogen for RT-PCR analysis of ETS1 and MYC expression. Humane endpoints were strictly followed, and no spontaneous animal deaths occurred during the study. Mice were housed in specific-pathogen-free conditions at 22–24 °C, 40–60% humidity, in individually ventilated cages with ad libitum access to sterilized food and water. Enrichment materials (nesting pads, gnawing sticks) were provided. All researchers completed mandatory animal handling and welfare training. All animal experimental procedures were performed in accordance with the Guide for the Care and Use of Laboratory Animals and were approved by the Ethics Committee of the Second Hospital of Shandong University (Approval No. KYLL2025289). Tumor measurements, body weight recordings, and behavioral assessments were performed by investigators blinded to group allocation. Treatment syringes were coded by an independent researcher, and the coding key was not disclosed to the assessment team until the completion of data analysis. Histopathological evaluation of HE-stained organ sections and RT-qPCR analysis of tumor tissues were conducted by pathologists and technicians who were unaware of the experimental groups. Statistical analysis was performed on coded datasets; the statistician remained blinded to group identities until the final interpretation stage.

Biodistribution Analysis

To evaluate the in vivo biodistribution and tumor-targeting efficiency of the nanoparticles, Cy5.5-labeled siRNA was encapsulated into both ETS1@Lip and ETS1@Lip-CAIX formulations using the identical microfluidic preparation protocol described above, yielding fluorescent nanoparticles with comparable physicochemical properties to their unlabeled counterparts. For biodistribution studies, tumor-bearing nude mice (established as described in the murine xenograft assay section) were randomized into two groups (n = 5 per group) and administered a single intravenous injection of Cy5.5-labeled ETS1@Lip or ETS1@Lip-CAIX at a dose of 1.5 mg siRNA/kg body weight via the tail vein. At 24 h post-injection, mice were euthanized under deep anesthesia (3% isoflurane), and major organs including the heart, liver, spleen, lungs, kidneys, and tumor tissues were carefully excised, rinsed with ice-cold PBS to remove residual blood, blotted dry, and weighed. Each tissue sample was homogenized in 1 mL of radioimmunoprecipitation assay (RIPA) buffer using a tissue grinder, followed by centrifugation at 12,000 × g for 10 min at 4°C to remove debris. The resulting supernatants were collected for fluorescence quantification.

Fluorescence intensity was measured using a SpectraMax iD3 Multi-Mode Microplate Reader (Molecular Devices) with excitation at 675 nm and emission at 694 nm. For each tissue sample, 200 μL of cleared supernatant was transferred in triplicate to a black 96-well plate (Corning) to minimize background autofluorescence. A standard curve was generated by serial dilution of free Cy5.5-siRNA in RIPA buffer (concentration range: 0.01–10 μg/mL, $R^2 > 0.99$) to ensure linear quantification. Tissue background autofluorescence was corrected by measuring parallel samples from untreated tumor-bearing mice and subtracting these values from the corresponding experimental readings. The total fluorescence content in each organ was calculated by multiplying the measured concentration by the total homogenate volume, and

subsequently normalized to tissue weight to yield fluorescence intensity per gram of tissue (FI/g). Targeting efficiency was assessed by calculating the tumor-to-liver and tumor-to-spleen fluorescence ratios for both nanoparticle formulations. All measurements were performed with automatic gain adjustment and 10 reads per well to ensure reproducibility.

Hematoxylin and Eosin Staining

At the endpoint of the in vivo therapeutic study, major organs including the liver, spleen, kidney, and heart were harvested from mice across all treatment groups. Tissues were immediately fixed in 10% neutral-buffered formalin for 48 h at room temperature, then dehydrated through a graded ethanol series (70%, 80%, 95%, and 100%, 1 h each), cleared in xylene, and embedded in paraffin wax. Serial sections of 4 μm thickness were cut using a rotary microtome (Leica RM2235), mounted onto positively charged glass slides, and dried at 60°C for 1 h.

For staining, sections were deparaffinized in xylene and rehydrated through descending ethanol concentrations (100%, 95%, 80%, and 70%, 3 min each), followed by a brief rinse in distilled water. Slides were stained with hematoxylin solution (G1120, Solarbio) for 5 min to visualize nuclei, differentiated in 1% acid alcohol for 10s, and blued in 0.5% ammonia water for 30s. After rinsing in running tap water for 5 min, sections were counterstained with eosin solution (G1100, Solarbio) for 3 min to visualize cytoplasmic and extracellular matrix components. Slides were then dehydrated through ascending ethanol concentrations (70%, 80%, 95%, and 100%, 2 min each), cleared in xylene and mounted with neutral balsam mounting medium. Cover slips were applied and sealed with nail polish.

Stained sections were examined under a light microscope (Olympus BX53) equipped with a digital camera (Olympus DP74). Histopathological evaluation was performed by a board-certified pathologist who was blinded to the experimental group allocation. Representative images were captured from at least five random fields per tissue section for documentation.

Statistical Analysis

All analyses were performed with GraphPad Prism 8.0. Data are presented as mean ± SD. qPCR results were analyzed by one-way ANOVA. MTT data were evaluated using two-way ANOVA (n = 3). Tumor weight and volume comparisons were analyzed by one-way ANOVA followed by Dunnett's test (n = 5 mice per group). $P < 0.05$ was considered statistically significant.

Results

ETS1 Is Overexpressed in ccRCC and Correlates with Poor Prognosis

To investigate the potential role of ETS1 in clear cell renal cell carcinoma (ccRCC), we first performed a bioinformatics analysis using public databases. Pan-cancer analysis revealed that ETS1 is significantly upregulated in various malignancies. Specifically, data from TCGA database demonstrated that ETS1 expression is remarkably higher in ccRCC tissues compared to normal kidney tissues (Figure 1A and B). Clinical significance was further assessed through survival analysis, which indicated that patients with high ETS1 expression had a significantly lower overall survival probability compared to those with low expression ($p = 0.00063$, Figure 1C).

To validate these findings, we performed RT-PCR on our clinical sample cohort. Consistent with the database results, ETS1 mRNA levels were significantly elevated in ccRCC tumor tissues compared to adjacent normal tissues (Figure 1D). Furthermore, we examined ETS1 expression in human ccRCC cell lines. Both 786-O and A-498 cells exhibited significantly higher ETS1 expression levels than the control cell line (UCL93) (Figure 1E).

To explore the biological function of ETS1 in ccRCC, we established cell models with ETS1 knockdown (via siETS1 #1 and #2) or overexpression (ETS1 OE). The efficiency of these modifications was confirmed at the protein level by Western blot analysis (Figure 1F and G). Cell proliferation assays demonstrated that overexpression of ETS1 significantly accelerated the growth of 786-O and A-498 cells. Conversely, silencing ETS1 remarkably inhibited cell proliferation in both cell lines (Figure 1H and I). These results collectively suggest that ETS1 acts as an oncogene in ccRCC by promoting tumor cell growth and is associated with poor patient outcomes.

https://doi.org/10.2147/IJN.S596277

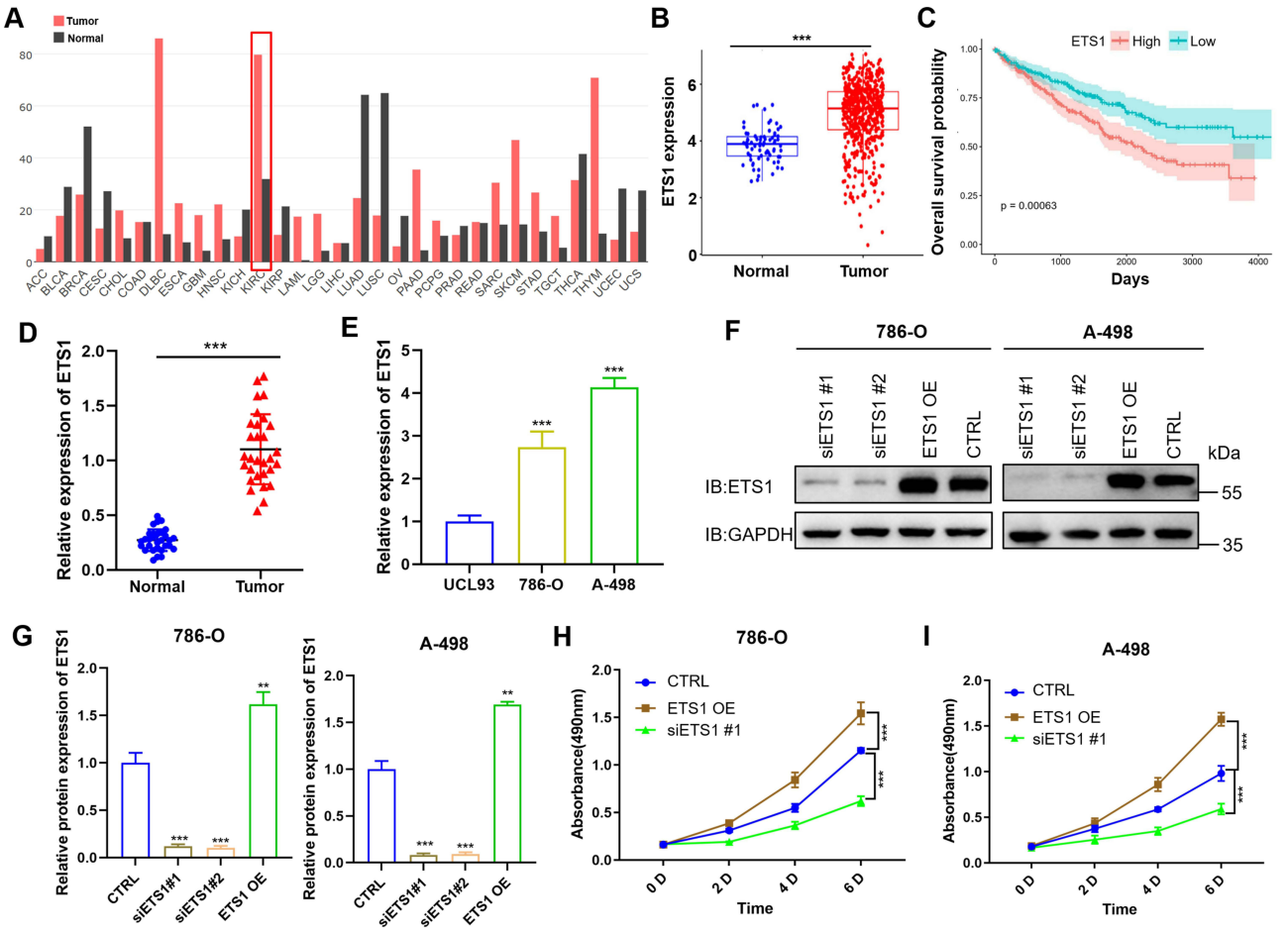

Figure 1 ETS1 is upregulated in ccRCC and correlates with poor patient prognosis. (**A**) Pan-cancer analysis of ETS1 expression across various malignancies. The red box highlights ETS1 expression in KIRC and adjacent normal tissues. (**B**) ETS1 expression levels in ccRCC and normal kidney tissues derived from TCGA database. (**C**) Kaplan-Meier survival analysis of ccRCC patients stratified by high and low ETS1 expression levels. (**D**) RT-PCR analysis of ETS1 mRNA levels in clinical ccRCC tumor tissues and adjacent normal tissues. (**E**) Relative mRNA expression of ETS1 in human ccRCC cell lines (786-O and A-498) compared with the control cell line (UCL93). (**F**) Western blot analysis confirming the efficiency of ETS1 knockdown (siETS1 #1 and #2) and overexpression (ETS1 OE) in 786-O and A-498 cells. (**G**) The protein quantification if ETS1 in (**F**). (**H** and **I**) MTT assay (measured by absorbance at 490 nm) showing the effects of ETS1 silencing or overexpression on the growth of 786-O (**H**) and A-498 (**I**) cells. **: p<0.01, ***: p < 0.001.

Single-Cell Transcriptomics Reveals Synergistic Activation of ETS1 and MYC in ccRCC

To further dissect the regulatory mechanisms, we analyzed the GSE178481 single-cell RNA-seq dataset. Unsupervised clustering followed by marker-based annotation identified major cellular populations, including tumor epithelial cells, normal epithelial cells, fibroblasts, myeloid cells, NK cells, T cells, B cells, endothelial cells, and a small unassigned population (Figure 2A). We next sought to identify the key transcriptional drivers operating specifically within the tumor epithelial cells. The resulting analysis revealed ETS1 and MYC as the top-ranked co-activated transcription factors within tumor epithelial cells. To visualize their functional interplay, we constructed a protein-protein interaction network using STRING, incorporating ETS1, MYC, and their validated first-order interacting partners retrieved with high confidence from the STRING database (Figure 2B). Using the VIPER algorithm, we observed that both ETS1 and MYC regulon activities were enriched in different cell populations (Figure 2C and D). Feature mapping at single-cell resolution showed that ETS1 expression was heterogeneous across the cellular landscape and was enriched in subsets of tumor-associated epithelial cells rather than uniformly distributed across all epithelial compartments. MYC exhibited a broader and more heterogeneous expression pattern across multiple cell populations (Figure 2C and D). These findings suggest that ETS1- and MYC-associated transcriptional programs are not restricted to a single uniform tumor-cell state, but instead vary across distinct cellular populations and epithelial subclusters within ccRCC.

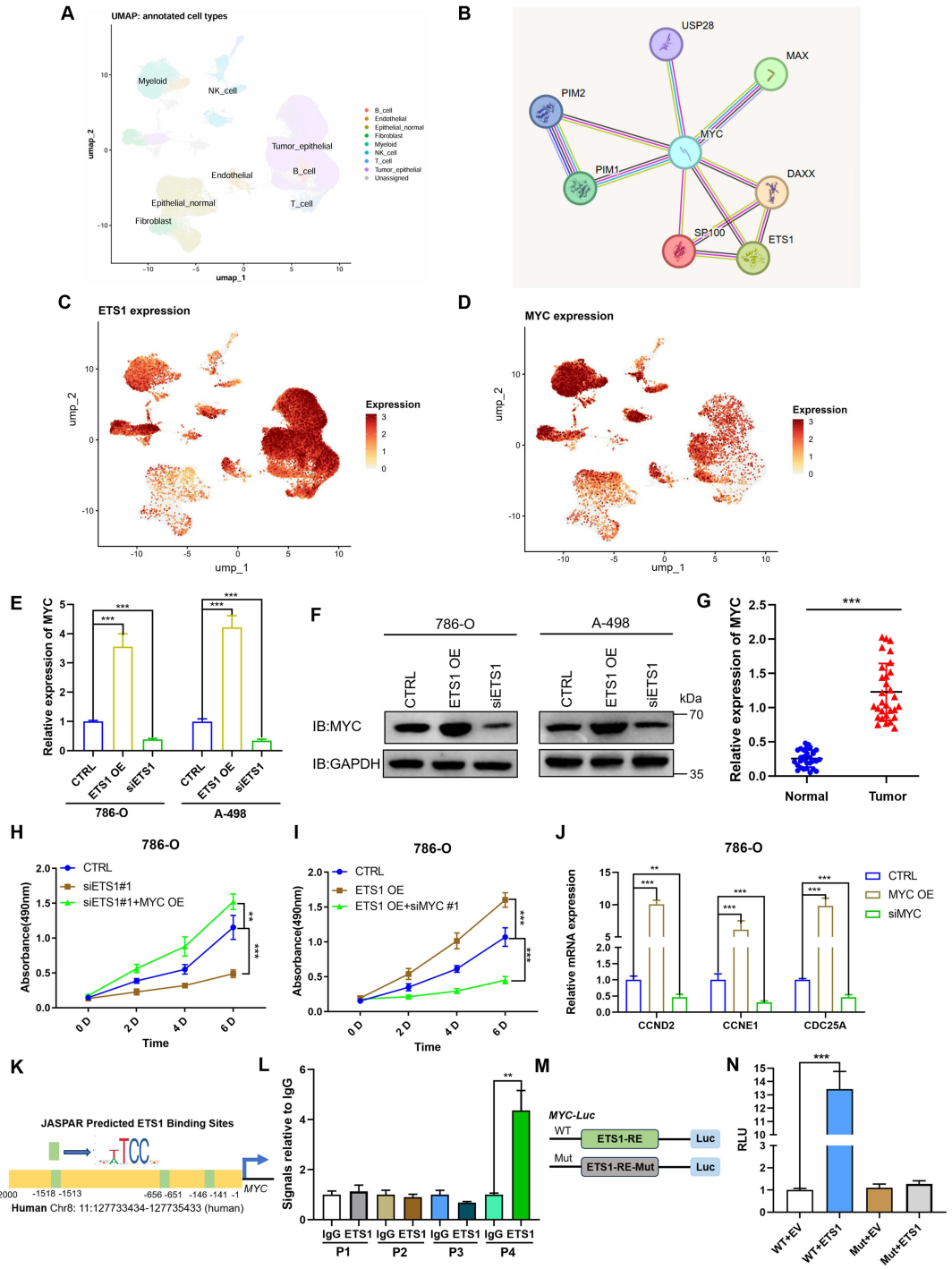

Figure 2 Single-cell transcriptomic analysis identifies ETS1 and MYC as synergistically activated drivers in ccRCC. (**A**) UMAP visualization of the GSE178481 single-cell RNA-seq dataset after unsupervised clustering and marker-based annotation, identifying major cell populations including tumor epithelial cells, normal epithelial cells, fibroblasts, myeloid cells, NK cells, T cells, B cells, endothelial cells, and a small unassigned population. (**B**) Protein-protein interaction network of the ETS1/MYC regulatory module in ccRCC. Network was constructed using STRING (v12.0) based on ETS1 and MYC (core TFs identified by VIPER analysis within the malignant epithelial cell subset) and their first-order interacting partners retrieved with high confidence (> 0.700) from experimental and database evidence. (**C**) UMAP feature plot showing ETS1 expression across the single-cell landscape. ETS1 exhibited heterogeneous expression across multiple cell populations, with enrichment in subsets of tumor-associated epithelial cells. (**D**) UMAP feature plot showing MYC expression across the single-cell landscape. MYC displayed a broader and heterogeneous distribution across multiple cellular compartments. (**E**) Quantitative RT-PCR analysis of MYC mRNA expression in 786-O and A-498 cells following ETS1 overexpression (ETS1 OE) or knockdown (siETS1). (**F**) Western blot analysis of MYC protein levels in ccRCC cell lines after modulation of ETS1 expression. (**G**) Relative mRNA expression of MYC in normal kidney tissues and ccRCC tumor tissues determined by RT-PCR. (**H**) MTT assay results showing that MYC overexpression partially rescues the growth inhibition induced by ETS1 silencing in 786-O cells. (**I**) MTT assay demonstrating that MYC knockdown significantly suppresses the accelerated cell growth caused by ETS1 overexpression in 786-O cells. (**J**) RT-PCR analysis of cell cycle-related genes (CCND2, CCNE1, CDC25A) following modulation of the MYC expression in 786-O cells. (**K**) Schematic representation of predicted ETS1 binding sites in the human MYC promoter region using the JASPAR database. (**L**) ChIP-PCR analysis validating the enrichment of ETS1 at the specific binding site (P4, −1518 to −1513 bp) within the MYC promoter in 786-O cells. (**M**) Schematic illustration of the wild-type (WT) and mutant (Mut) *MYC* promoter luciferase reporter constructs. (**N**) Dual-luciferase reporter assay confirming that ETS1 promotes MYC transcription through the identified binding site in 786-O cells. ** $p < 0.01$; *** $p < 0.001$.

https://doi.org/10.2147/IJN.S596277

Crucially, detailed analysis of cluster composition confirmed a significant overlap of ETS1 and MYC expression. We observed a substantial fraction of cells exhibiting high activity for both ETS1 and MYC across multiple clusters (Supplementary Figure 1A). The distribution of regulon activity scores further highlighted the synchronized activation of these two factors across the identified cell identities (Supplementary Figure 1B). Additionally, a marker dot plot confirmed that ETS1 and MYC were consistently expressed alongside canonical tumor markers in relevant clusters (Supplementary Figure 1C).

We then validated the ETS1-MYC axis experimentally. In ccRCC cell lines, RT-PCR and Western blot analyses demonstrated that ETS1 overexpression significantly upregulated MYC expression, whereas ETS1 knockdown led to a marked decrease in MYC levels at both mRNA and protein levels (Figure 2E, F and Supplementary Figure 2A). Clinical sample analysis showed that MYC expression was also significantly higher in ccRCC tumors than in normal tissues (Figure 2G). These results suggest that ETS1 promotes ccRCC progression by positively regulating MYC.

To further confirm that ETS1 affects ccRCC progression through MYC, we performed MYC overexpression experiments in the context of ETS1 knockdown (Supplementary Figure 2B and C). MTT assay results revealed that overexpressing MYC partially rescued the proliferation inhibition caused by ETS1 silencing and accelerated the growth rate of ccRCC cells (Figure 2H and Supplementary Figure 2D). Conversely, knocking down MYC in ETS1-overexpressing cells significantly suppressed cell growth (Figure 2I and Supplementary Figure 2E). These findings further indicate that ETS1 exerts its biological effects in ccRCC through MYC. Previous reports have established that MYC regulates cell proliferation by influencing the cell cycle.[14–16] RT-PCR analysis of key cell cycle regulatory genes showed that MYC overexpression in ccRCC significantly promoted cell cycle progression (Figure 2J and Supplementary Figure 2F).

As a transcription factor, we hypothesized that ETS1 might bind to the MYC promoter region to enhance its transcription. JASPAR predictions identified several potential ETS1 binding sites within the MYC promoter (Figure 2K). ChIP-PCR assays subsequently confirmed that ETS1 directly binds to a specific region (−1518 to −1513 bp) of the MYC promoter (Figure 2L). To further validate this interaction, dual-luciferase reporter assays were performed (Figure 2M). The results demonstrated that ETS1 failed to promote gene transcription once this binding region was mutated (Figure 2N). Taken together, these results demonstrate that ETS1 promotes ccRCC progression by directly enhancing MYC transcription and subsequently accelerating the cell cycle.

Design and Validation of an Optimized CA9-Targeting Peptide CaIX-P7

Following the discovery of the ETS1/MYC regulatory axis as a driver of ccRCC progression, we sought to develop a delivery platform capable of precisely transporting therapeutic siRNA to these malignant cells. To achieve high tumor specificity and minimize off-target effects, we focused on Carbonic Anhydrase IX (CA9). While many oncogenic drivers are intracellular, CA9 is uniquely suited for targeted nanomedicine due to its robust extracellular domain expression and high tumor specificity in the context of ccRCC. Crucially, CA9 expression remains minimal in healthy renal compartments, providing a clear therapeutic window for site-specific delivery. Based on these findings, we proceeded to optimize a CA9-specific targeting ligand to functionalize our liposomal carrier.[3,4]

We employed a computational optimization workflow starting with the original peptide CaIX-P1 which has been reported that could bind CA9 (Figure 3A). Through molecular docking with HADDOCK and interface binding energy (ΔG) analysis, we performed mutation screening to enhance binding affinity. This systematic in silico screening pipeline identified 10 candidate peptides with predicted affinity enhancements, from which CaIX-P7 (sequence: WNTNHVPLSPRY) was selected based on the favorable combined HADDOCK score, mCSM-PPI2 ΔΔG prediction (−1.24 kcal/mol), and experimental validation via SPR and cellular uptake assays (Figure 3A). Our RT-PCR results confirmed that CA9 was highly expressed in ccRCC (Figure 3B).

To evaluate the binding affinity and competitive potential of CaIX-P7, we synthesized biotin-conjugated CaIX-P1 for use in competitive binding assays. The results demonstrated that increasing concentrations of CaIX-P7 effectively displaced Biotin-CaIX-P1 in a dose-dependent manner, indicating a superior competitive binding capacity for the CA9 protein (Supplementary Figure 3A). The binding affinity of the peptides to CA9 protein was further validated using SPR. The results demonstrated that CaIX-P7 exhibited a significantly lower dissociation constant (Kd=52.96 nM) compared to the original CaIX-P1 (Kd=226.52 nM), indicating a nearly four-fold increase in binding affinity (Figure 3C and D). Furthermore, cellular

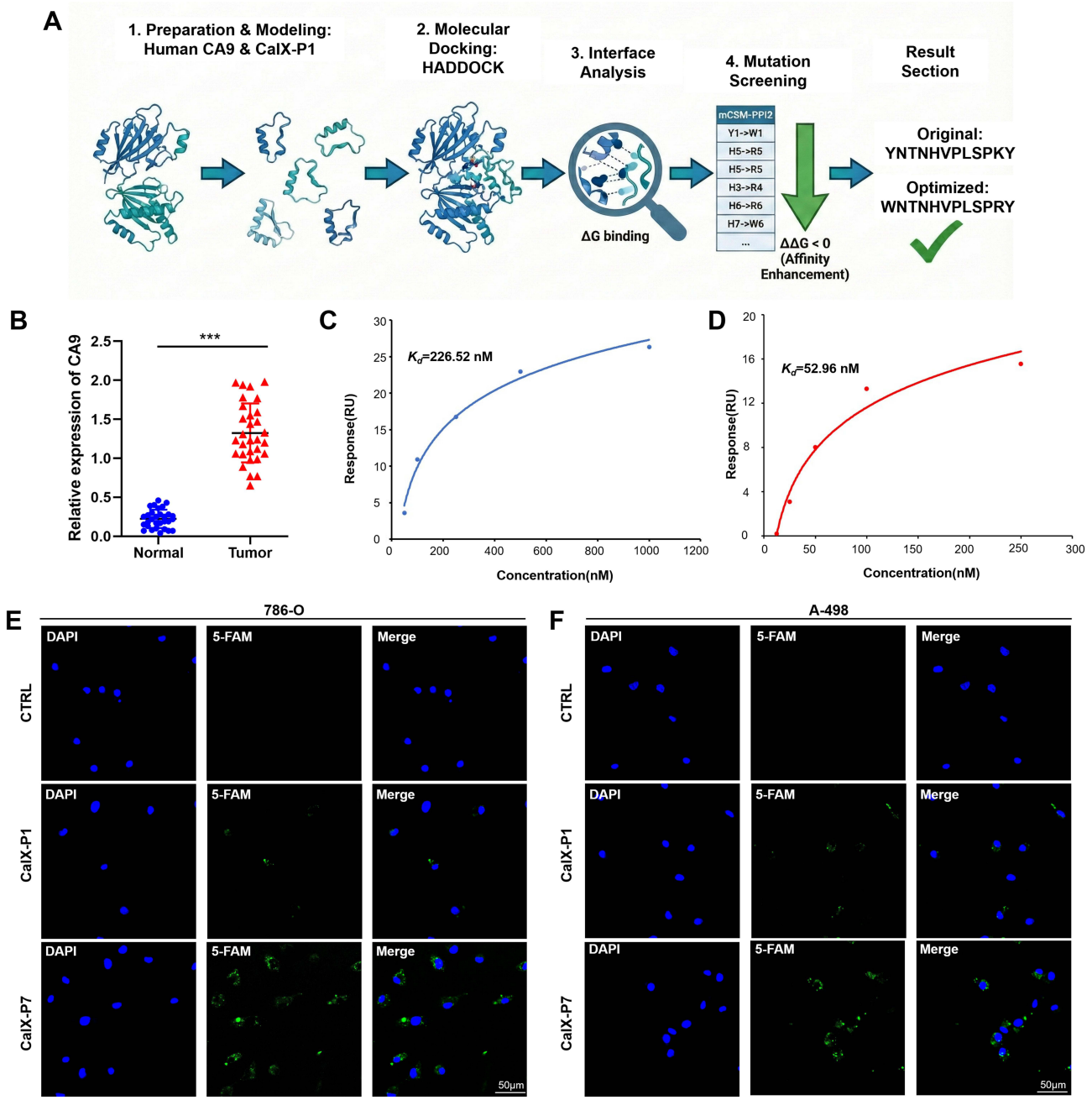

Figure 3 Design and validation of the optimized CA9-targeting peptide CaIX-P7. (**A**) Schematic workflow of the CA9-targeting peptide optimization. (**B**) RT-PCR analysis showing significantly higher CA9 mRNA levels in ccRCC tumor tissues compared to adjacent normal tissues. (**C** and **D**) SPR affinity curves for the binding of CaIX-P1 (Kd = 226.52 nM) (**C**) and CaIX-P7 (Kd = 52.96 nM) (**D**) to recombinant CA9 protein. (**E** and **F**) Representative fluorescence images of 786-O (**E**) and A-498 (**F**) cells incubated with 5-FAM labeled CaIX-P1 or CaIX-P7 (green). Nuclei were counterstained with DAPI (blue). ***: $p < 0.001$.

uptake experiments were conducted in 786-O and A-498 cell lines using 5-FAM labeled peptides. Fluorescence microscopy revealed that cells treated with CaIX-P7 exhibited markedly stronger green fluorescence compared to those treated with CaIX-P1, confirming the superior binding and internalization capability of the optimized peptide in ccRCC cells (Figure 3E and F). To further verify the specificity of the interaction between CaIX-P7 and CA9, we performed knockdown experiments targeting CA9 in ccRCC cell lines (Supplementary Figure 3B and C). Immunofluorescence analysis revealed that the binding of CaIX-P7 to the cell surface was significantly diminished following CA9 silencing (Supplementary Figure 3D and E). These findings provide robust evidence that CaIX-P7 specifically targets and binds to CA9, supporting its potential as an optimized ligand for targeted delivery in ccRCC therapy.

https://doi.org/10.2147/IJN.S596277

Preparation and Characterization of CA9-Targeted Liposomal Nanoparticles

To achieve the targeted delivery of siETS1 to ccRCC cells, we developed a functionalized liposomal nanoparticle system, named ETS1@Lip-CAIX. The synthesis process employed a microfluidic mixing technique to encapsulate siETS1 within a lipid bilayer, followed by surface conjugation with the optimized CaIX-P7 peptide via thiol-maleimide chemistry (Figure 4A). Transmission electron microscopy (TEM) images revealed the typical morphology of ETS1@Lip-CAIX, which exhibited a spherical shape with a relatively uniform size distribution (Figure 4B). Characterization using DLS revealed that the empty liposomes (CTRL) and siETS1-loaded liposomes (ETS1@Lip) exhibited uniform hydrodynamic sizes of 102.3 nm and 122.5 nm, respectively. Upon conjugation with the CaIX-P7 peptide, the particle size of ETS1@Lip-CAIX increased to 154.8 nm, reflecting the successful integration of the targeting ligand (Figure 4C–E).

The nanoparticles displayed a low PDI (0.128 for ETS1@Lip and 0.146 for ETS1@Lip-CAIX) and a high nucleic acid encapsulation efficiency (95.4% and 89.1%, respectively), indicating a stable and homogeneous formulation

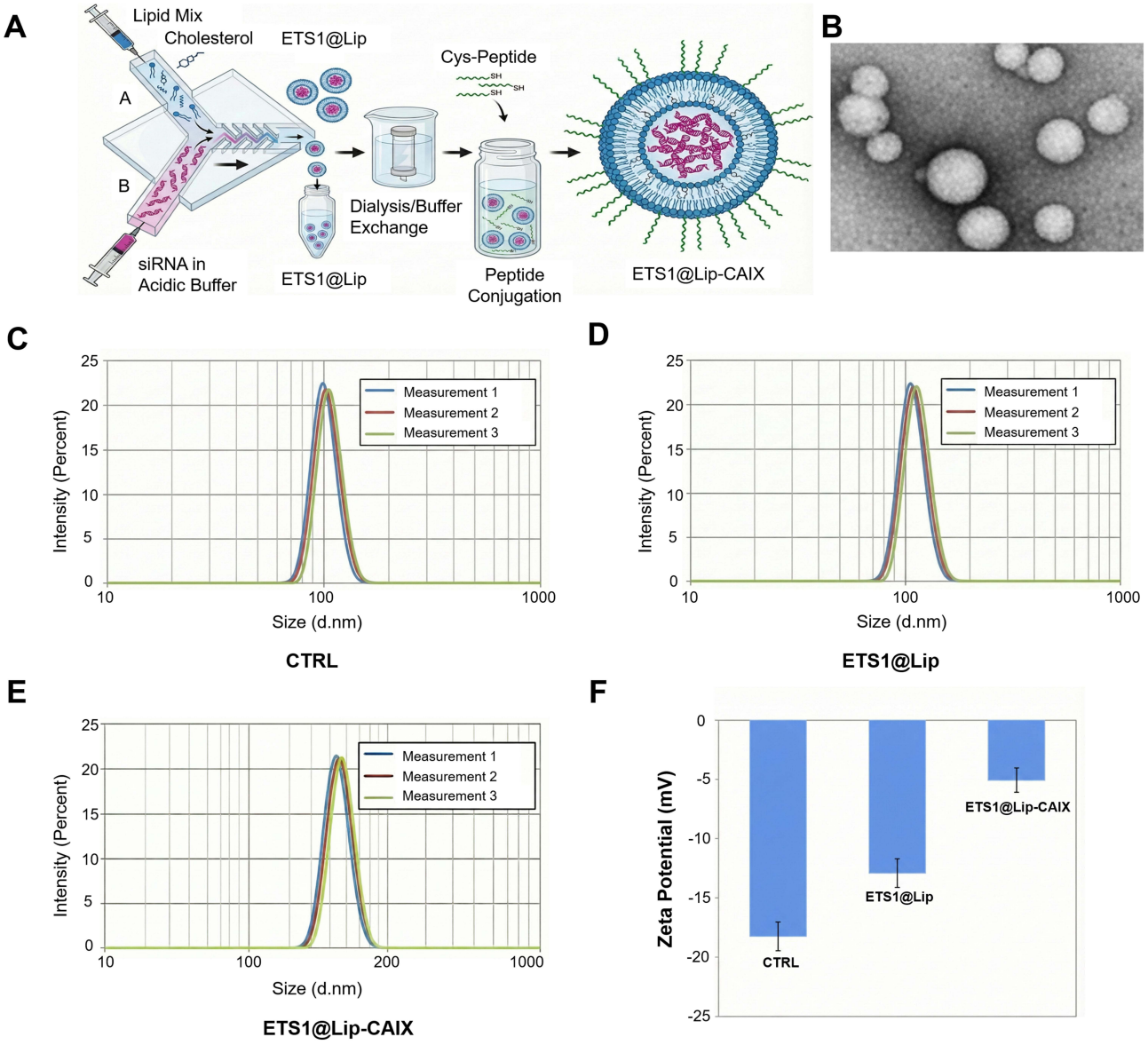

Figure 4 Design, synthesis, and characterization of the targeted liposomal nanoparticle ETS1@Lip-CAIX. (**A**) Schematic illustration of the microfluidic-based synthesis process for ETS1@Lip-CAIX. (**B**) Representative TEM image of ETS1@Lip-CAIX, showing a spherical morphology and relatively uniform size distribution. (**C**–**E**) Representative size distribution profiles of empty liposomes (CTRL) (**C**), ETS1@Lip (**D**), and ETS1@Lip-CAIX (**E**) as determined by DLS. (**F**) Zeta potential measurements of empty liposomes (CTRL), ETS1@Lip, and ETS1@Lip-CAIX.

(Table S4). The peptide conjugation efficiency during the functionalization process was determined to be 72.4% (Table S4). Furthermore, zeta potential measurements showed a progressive shift in surface charge from approximately −18.3 mV for empty liposomes to −13.0 mV for ETS1@Lip, and further to −5.1 mV for ETS1@Lip-CAIX (Figure 4F). This increase in zeta potential confirms the successful surface modification with the positively charged CaIX-P7 peptides, providing a structural basis for enhanced tumor-targeting capability.

To further confirm the protective effect of the liposomes on siRNA, nanoparticles were treated with RNase followed by neutralization with EDTA. RiboGreen assay results demonstrated that the liposomal carrier effectively maintained the integrity of the encapsulated siRNA against enzymatic degradation (Supplementary Figure 4A). Stability assays further showed that ETS1@Lip-CAIX remained stable in serum at 37°C for over 48 h (Supplementary Figure 4B) and at 4°C for more than 14 days (Supplementary Figure 4C). Subsequently, we investigated the drug release kinetics of the nanoparticles. Under physiological conditions (pH 7.4), both ETS1@Lip and ETS1@Lip-CAIX exhibited high stability, with less than 20% of the total siRNA released within 24 h (Supplementary Figure 4D and E). In contrast, a rapid release of siRNA was observed under acidic conditions (pH 5.5) (Supplementary Figure 4D and E), suggesting that the nanoparticles are designed for responsive cargo release within the endo-lysosomal compartments.

ETS1@Lip-CAIX Inhibits ccRCC Growth by Downregulating ETS1 and MYC Expression

To evaluate the therapeutic potential and targeting specificity of the functionalized nanoparticles, we treated ccRCC cell lines with ETS1@Lip and ETS1@Lip-CAIX. RT-PCR analysis revealed that both formulations significantly downregulated ETS1 mRNA levels in 786-O and A-498 cells compared to the control group. Notably, the targeted ETS1@Lip-CAIX achieved superior silencing efficiency over the non-targeted ETS1@Lip, highlighting the enhanced cellular uptake mediated by the CaIX-P7 peptide (Figure 5A). Consistent with the regulatory axis identified earlier, a significant decrease in MYC expression was also observed following the knockdown of ETS1 via nanoparticle delivery (Figure 5B).

In terms of biological impact, cell proliferation assays demonstrated that ETS1@Lip-CAIX markedly inhibited the growth of 786-O and A-498 cells (Figure 5C). While the non-targeted ETS1@Lip showed some degree of inhibition, the effect was significantly less pronounced than that of the targeted formulation (Figure 5C). To further assess the safety profile and tumor-targeting specificity, the nanoparticles were tested on normal UCL93 cells (Figure 5D). Importantly, no significant growth inhibition was observed in any treatment group for UCL93 cells (Figure 5D). We further examined the potential cytotoxicity of the delivery vehicle and the specificity of the gene-silencing effect. Treatment with empty nanoparticles (Blank LNP), Scrambled siRNA-loaded nanoparticles (Scrambled@Lip), or CA9-targeted Scrambled siRNA-loaded nanoparticles (Scrambled@Lip-CAIX) had no significant impact on the proliferation of 786-O, A-498, and UCL93 cell lines (Supplementary Figure 5A–C). These results indicate that the observed growth inhibition is specifically attributed to the siETS1 cargo rather than the nanoparticle components or non-specific siRNA sequences.

ETS1@Lip-CAIX Suppresses the Growth of Patient-Derived ccRCC Organoids

To further evaluate the therapeutic efficacy of ETS1@Lip-CAIX in a more clinically relevant model, we established patient-derived organoids (PDOs) from human ccRCC specimens. The organoids were successfully cultured and monitored for growth over 7 days, during which they formed stable 3D structures (Figure 6A). Subsequently, we assessed the inhibitory effects of ETS1@Lip and ETS1@Lip-CAIX on two independent PDO lines (#1 and #2).

Morphological observation revealed that the organoids in the control group (CTRL) exhibited healthy growth with increasing diameters (Figure 6B and C). However, treatment with ETS1@Lip and ETS1@Lip-CAIX significantly impaired organoid development. Specifically, the average diameter of the organoids was markedly reduced in the treatment groups compared to the CTRL group, with ETS1@Lip-CAIX demonstrating the most potent inhibitory effect (Figure 6B and C). Furthermore, cell viability analysis showed that ETS1@Lip-CAIX treatment led to a significant increase in the percentage of cell death within the organoid population compared to the non-targeted ETS1@Lip group (Figure 6B and C). Consistently, the expression levels of ETS1 and MYC were significantly downregulated in both PDO lines following ETS1@Lip-CAIX

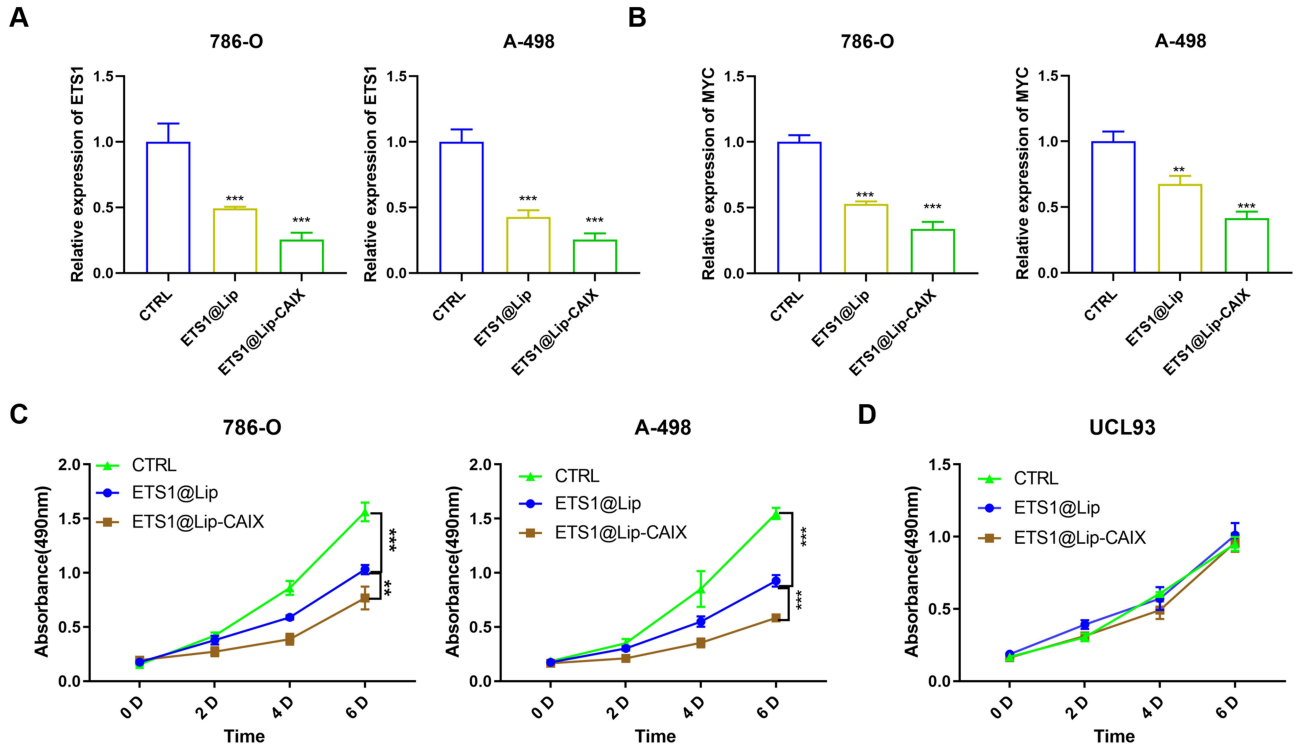

Figure 5 ETS1@Lip-CAIX inhibits ccRCC growth through targeted downregulation of the ETS1/MYC axis. (**A**) Relative mRNA expression of ETS1 in 786-O and A-498 cells following treatment with ETS1@Lip and ETS1@Lip-CAIX. (**B**) Relative mRNA expression of MYC in ccRCC cell lines after treatment with the indicated nanoparticles. (**C**) Cell proliferation curves showing the inhibitory effects of ETS1@Lip and ETS1@Lip-CAIX on the growth of 786-O and A-498 cells. (**D**) Cell proliferation curves of normal UCL93 cells treated with ETS1@Lip and ETS1@Lip-CAIX, demonstrating minimal cytotoxicity toward non-cancerous cells. ** p<0.01, *** p<0.001.

treatment (Supplementary Figure 6A–D). These results indicate that ETS1@Lip-CAIX effectively inhibits the growth of ccRCC in a patient-derived organoid model through targeted downregulation of the ETS1/MYC axis.

ETS1@Lip-CAIX Inhibits ccRCC Growth in vivo

To further evaluate the therapeutic potential of ETS1@Lip-CAIX in vivo, we established subcutaneous xenograft models in nude mice using two distinct ccRCC cell lines, 786-O and A-498. Following the successful establishment of tumors, mice were treated with saline (CTRL), non-targeted ETS1@Lip, or targeted ETS1@Lip-CAIX.

In both the 786-O and A-498 models, treatment with ETS1@Lip-CAIX resulted in the most significant inhibition of tumor progression compared to the CTRL and ETS1@Lip groups (Figure 7A and F). Longitudinal monitoring of tumor growth curves revealed a marked retardation in tumor volume increase in the ETS1@Lip-CAIX treatment group for both cell lines (Figure 7B and G). Statistical analysis of the harvested tumors confirmed a substantial reduction in both terminal tumor volume and weight following ETS1@Lip-CAIX administration in both the 786-O model (Figure 7C and D) and the A-498 model (Figure 7H and I). Importantly, throughout the treatment period, no significant differences in body weight were observed between the nanoparticle-treated groups and the control group in either xenograft model (Supplementary Figure 7A and B).

To confirm the molecular mechanism underlying this growth inhibition in vivo, we assessed ETS1 expression within the tumor tissues. Quantitative RT-PCR analysis demonstrated that ETS1@Lip and ETS1@Lip-CAIX effectively silenced ETS1 mRNA levels in tumors derived from both 786-O (Figure 7E) and A-498 (Figure 7J) cells. Consistently, the expression of the downstream target MYC was also significantly downregulated in these xenograft tumors following treatment (Supplementary Figure 7D and E). These findings collectively demonstrate that the CA9-targeted delivery of siETS1 via ETS1@Lip-CAIX provides a robust therapeutic strategy for inhibiting ccRCC growth in vivo.

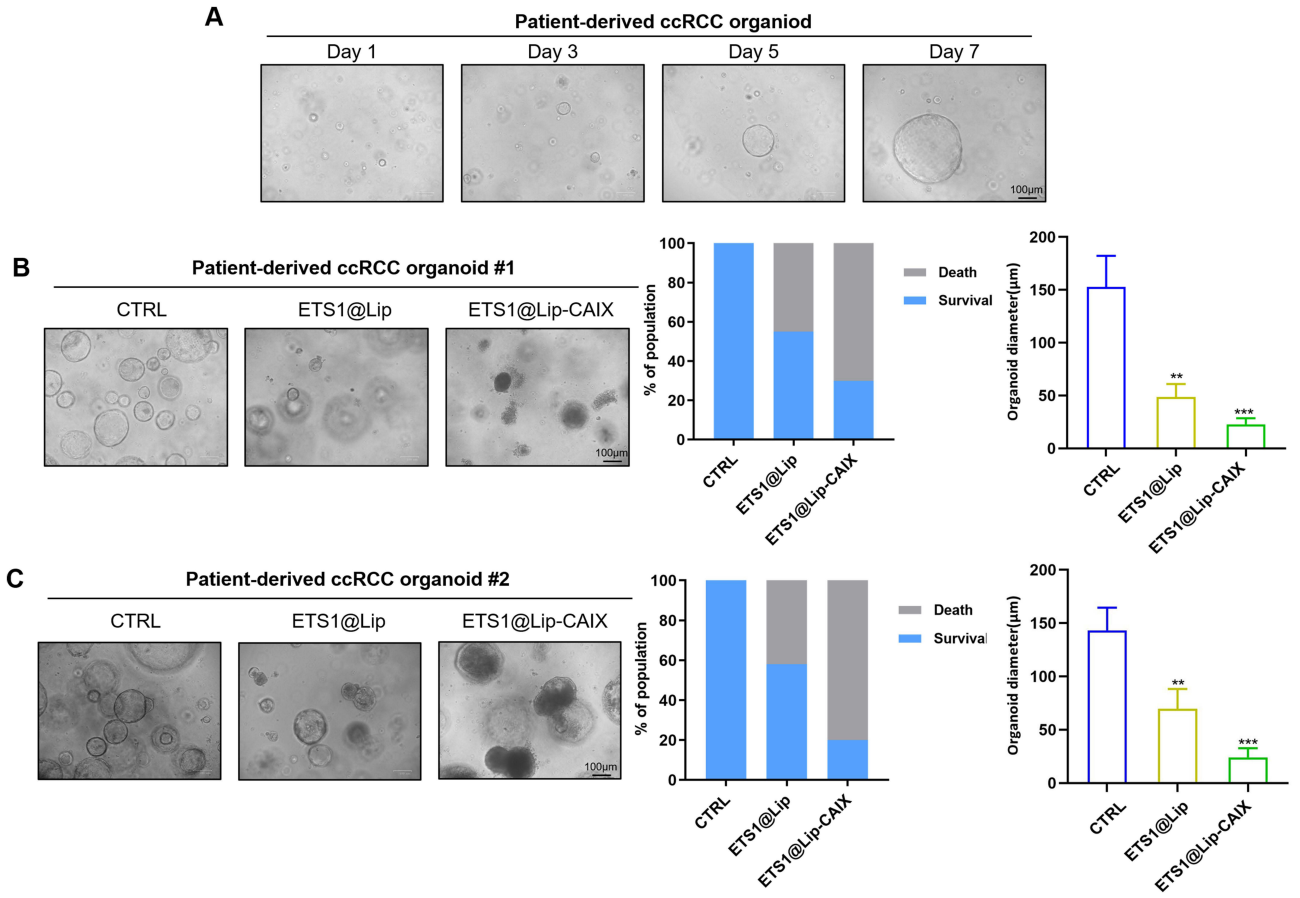

Figure 6 ETS1@Lip-CAIX inhibits the growth of patient-derived ccRCC organoids. (**A**) Representative bright-field images showing the establishment and morphological progression of patient-derived ccRCC organoids from Day 1 to Day 7. (**B** and **C**) Therapeutic evaluation of ETS1@Lip and ETS1@Lip-CAIX in two patient-derived ccRCC organoid lines, #1 (**B**) and #2 (**C**). **: p<0.01, ***: p<0.001.

ETS1@Lip-CAIX Suppresses the Growth of Patient-Derived ccRCC Organoids in vivo

To further validate the translational potential of ETS1@Lip-CAIX, we established a more clinically relevant xenograft model using patient-derived ccRCC organoids. Consistent with the findings in cell line-derived models, ETS1@Lip-CAIX treatment exhibited potent anti-tumor activity in the organoid-derived xenografts, as evidenced by the significantly smaller size of excised tumors in the targeted treatment group (Figure 8A). Tumor growth curve revealed that ETS1@Lip-CAIX markedly retarded the growth of the tumors compared to both the control and non-targeted ETS1@Lip groups (Figure 8B).

Quantitative assessments at the study endpoint confirmed that both terminal tumor volume (Figure 8C) and weight (Figure 8D) were significantly reduced following ETS1@Lip-CAIX administration. Throughout the therapeutic window, the body weight of mice in the nanoparticle-treated groups remained stable, with no significant differences observed compared to the control group (Supplementary Figure 7C). Furthermore, RT-PCR analysis of the tumor tissues demonstrated that the targeted nanoparticles successfully silenced the expression of ETS1 mRNA and decreased the expression of MYC in vivo (Figure 8E and Supplementary Figure 7F). To elucidate the mechanism underlying the enhanced therapeutic efficacy, we investigated the systemic biodistribution of the nanoparticles. Tissue analysis revealed that the non-targeted ETS1@Lip primarily accumulated in the liver and spleen. In contrast, the CA9-targeted ETS1@Lip-CAIX demonstrated superior tumor-homing capabilities, with significantly higher accumulation in the tumor site (Figure 8F). This targeted enrichment facilitates precise tumor killing while minimizing off-target effects. Furthermore, histological evaluation via H&E staining showed no discernible morphological alterations or pathological damage in the major organs

https://doi.org/10.2147/IJN.S596277

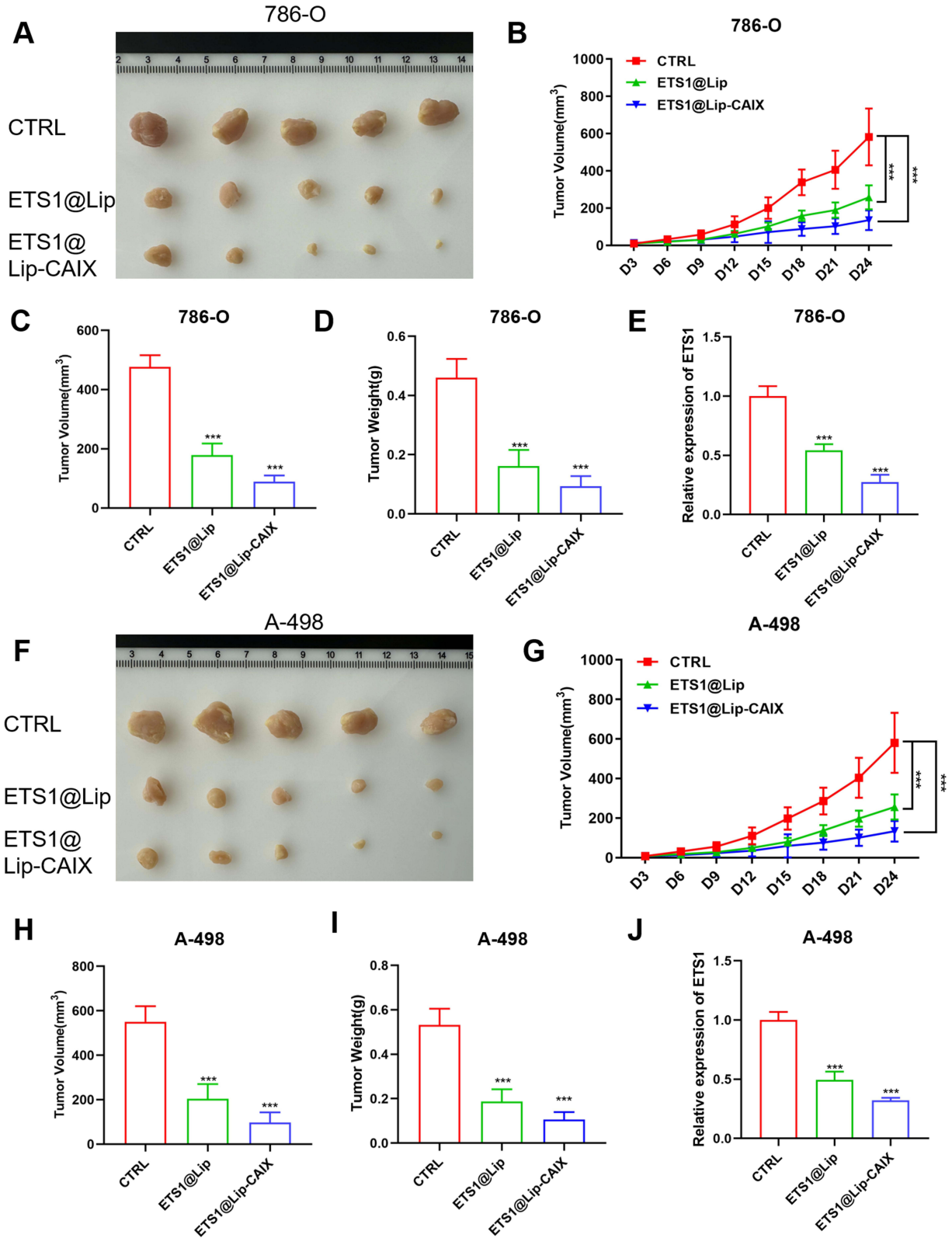

Figure 7 ETS1@Lip-CAIX suppresses ccRCC tumor growth in both 786-O and A-498 xenograft models. (**A**) Representative images of subcutaneous tumors derived from 786-O cells (n = 5 mice per group). (**B**) Tumor growth curves of 786-O xenografts. (**C** and **D**) Statistical analysis of terminal tumor volume (**C**) and tumor weight (**D**) for the 786-O xenograft model. (**E**) Relative mRNA expression of ETS1 in 786-O tumor tissues determined by RT–PCR analysis. (**F**) Representative images of subcutaneous tumors derived from A-498 cells (n = 5 mice per group). (**G**) Tumor growth curves of A-498 xenografts. (**H** and **I**) Statistical analysis of terminal tumor volume (**H**) and tumor weight (**I**) for the A-498 xenograft model. (**J**) Relative mRNA expression of ETS1 in A-498 tumor tissues. *** p<0.001.

https://doi.org/10.2147/IJN.S596277

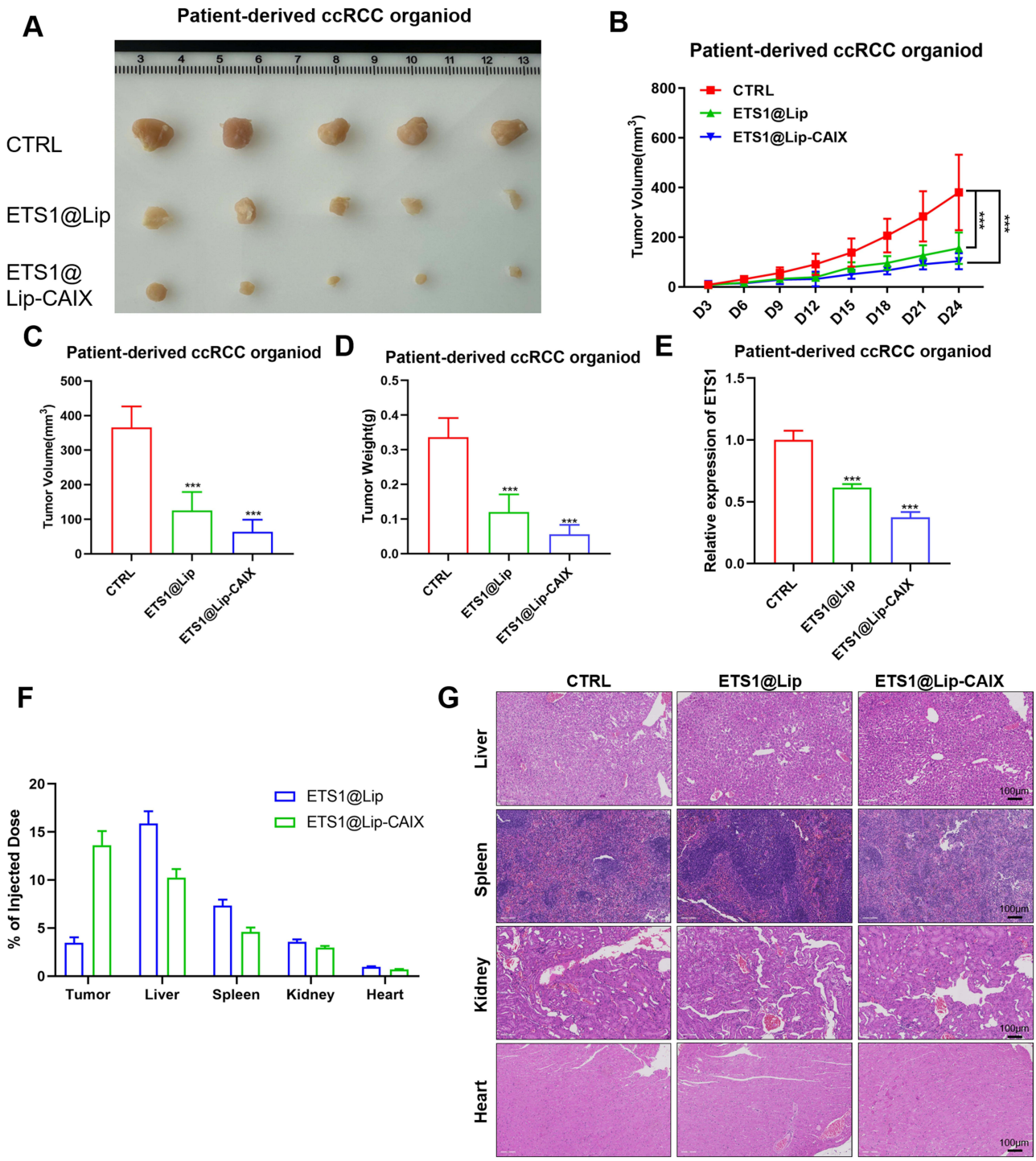

Figure 8 ETS1@Lip-CAIX suppresses the growth of patient-derived ccRCC organoids in vivo. (**A**) Representative images of subcutaneous xenograft tumors derived from patient-derived ccRCC organoids. (**B**) Tumor growth curves showing the progression of organoid-derived xenografts across the indicated treatment groups (n = 5 per group). (**C** and **D**) Statistical analysis of terminal tumor volume (**C**) and tumor weight (**D**) for the organoid-derived xenograft model. (**E**) Relative mRNA expression levels of ETS1 in the tumor tissues as determined by RT-PCR analysis. (**F**) In vivo biodistribution and tumor-targeting efficiency of Cy5.5-labeled nanoparticles. (**G**) Histopathological evaluation of major organs following nanoparticle treatment. ***: $p < 0.001$.

(liver, spleen, kidney and heart) across both nanoparticle treatment groups (Figure 8G). These findings collectively underscore the high biosafety profile and the robust tumor-targeting efficiency of the ETS1@Lip-CAIX system, supporting its potential for the management of advanced ccRCC.

https://doi.org/10.2147/IJN.S596277

Discussion

ccRCC is the most prevalent and aggressive histological subtype of kidney cancer, accounting for approximately 75–80% of all primary renal malignancies.[17] Despite advancements in surgical techniques and systemic therapies, the prognosis for patients with advanced or metastatic ccRCC remains unsatisfactory due to high recurrence rates and the development of therapeutic resistance.[1,2] Consequently, identifying novel molecular drivers and developing precision delivery systems are essential for improving patient outcomes.

Through the analysis of TCGA databases and clinical samples, this study established the significant overexpression of ETS1 in ccRCC and its marked correlation with poor patient prognosis. As a core member of the ETS transcription factor family, ETS1 is recognized for its role in regulating epithelial-mesenchymal transition, angiogenesis, and apoptosis in various malignancies.[18–21] In the context of ccRCC, our experiments confirmed that ETS1 gain-of-function (overexpression) significantly accelerates tumor cell growth, whereas its loss-of-function (knockdown) produces the opposite effect, further consolidating its status as a key oncogenic driver. Utilizing scRNA-seq and the VIPER algorithm, we observed a high degree of synchrony and spatial overlap in ETS1 and MYC regulon activities within tumor cell populations. This synergistic activation at the single-cell level implies a tight regulatory logic between these two transcription factors in maintaining the malignant phenotype. Experimental validation demonstrated that ETS1 positively modulates MYC expression at both the mRNA and protein levels. As a universal oncogenic transcription factor, MYC drives cell cycle progression, metabolic reprogramming, and biomass synthesis.[14–16] CHIP-PCR and dual luciferase assays confirmed that ETS1 could affect ccRCC by regulating transcription of MYC. Therefore, the regulation of MYC by ETS1 elucidates how elevated ETS1 levels confer a potent proliferative advantage in ccRCC. Previous studies have demonstrated that the overexpression of ETS1 in ccRCC not only accelerates tumor proliferation but also promotes the recruitment and enrichment of immunosuppressive macrophages, a finding that is highly consistent with the oncogenic role of ETS1 observed in our present study.[22] Furthermore, Qian et al[7] identified ETS1 as a pivotal mediator of acquired drug resistance in ccRCC. Mechanistically, HDAC8 facilitates the deacetylation of ETS1 at the K245 residue, which strengthens its interaction with HIF-2α. The resulting ETS1/HIF-2α complex subsequently reduces the sensitivity of ccRCC cells to tyrosine kinase inhibitors, such as sunitinib.[7] These collective findings underscore the therapeutic potential of targeting the ETS1 axis to overcome both tumor progression and therapeutic resistance.

To therapeutically target this regulatory axis, we successfully engineered a CA9-targeted nanoplatform. Under normal physiological conditions, CA9 expression is minimal in healthy renal tissues; however, it is characteristically overexpressed on the cell surface in ccRCC.[23,24] Our results confirmed that CA9 mRNA levels in ccRCC tumor tissues are significantly higher than those in adjacent normal tissues. Given its cell-surface localization and high tumor specificity, CA9 is considered an ideal anchor for site-specific drug delivery in ccRCC. To date, numerous CA9-targeted nanoplatforms have been developed for the diagnosis and treatment of RCC. Fukushima et al[24] developed a theranostic system by conjugating an anti-CA9 monoclonal antibody with the near-infrared dye IR700. This platform achieved exceptional tumor accumulation in ccRCC models and facilitated the specific eradication of CA9-positive tumor cells via near-infrared photoimmunotherapy while sparing the surrounding normal renal parenchyma. In another approach, Alsaab et al[25] utilized acetazolamide as a small-molecule ligand to functionalize sorafenib-loaded polymeric nanoparticles. These nanoparticles precisely targeted CA9 in hypoxic regions, enhancing drug penetration into the tumor core and overcoming therapeutic resistance by modulating tumor-associated macrophages. Furthermore, a hydroxyethyl starch-based nanoplatform (CHHD-Cu NPs) conjugated with a CA9 inhibitor was designed to integrate doxorubicin-mediated chemotherapy with Cu^{2+}-mediated chemodynamic therapy.[26] This multi-modal system effectively eliminated CA9-expressing cancer stem cells and demonstrated robust anti-tumor efficacy across various malignancies. Beyond RCC, CA9-targeted nanoparticles have also been extensively investigated in other pathologies, including lung cancer, osteoarthritis, and breast cancer.[27–29]

Another advantage of this study lies in its high clinical relevance. To bridge the gap between in vitro experiments and clinical application, we established patient-derived organoids from surgically resected ccRCC specimens as a more physiologically relevant experimental model. Unlike traditional 2D cell lines, PDOs preserve the complex 3D architecture and genetic heterogeneity of the primary tumor, providing a robust platform for evaluating drug penetration and therapeutic efficacy.[30,31] Zheng et al[32,33] utilized clinical patient-derived colorectal cancer organoids to robustly validate the efficacy of

nanoparticles in targeting R-spondin and activating the cGAS-STING signaling pathway. However, there have been no reports on the use of ccRCC organoids to evaluate nanoparticle performance. In the present study, treatment with ETS1@Lip-CAIX significantly impaired organoid growth, as evidenced by a marked reduction in organoid diameter and a substantial increase in cell death across multiple independent PDO lines. This growth inhibition was mechanistically supported by the effective downregulation of the ETS1/MYC regulatory axis within these complex 3D architectures.

Furthermore, a diverse array of organoid models including intestinal, lung, liver, oral squamous cell carcinoma, and cardiac organoids has been extensively employed to assess the efficacy and safety of various nanoplatforms.[34–38] Wang et al[34] leveraged an oral squamous cell carcinoma sample library to verify the effectiveness of a pH-sensitive nanoparticle for siCDCP1 delivery, establishing PDOs as robust preclinical models for mechanistic exploration and therapeutic development. Similarly, Grumelot et al[35] utilized human iPSC-derived cardiac organoids to investigate nanoparticle distribution and the co-localization of cardiomyocytes (CMs) and epicardial cells, revealing the critical role of CMs in nanoparticle-mediated cardiac therapies. Their findings suggest that incorporating additional features, such as immune system components, would more accurately simulate native cardiac tissue and enhance the utility of organoids in studying drug-nanoparticle interactions.[35] Additionally, respiratory organoids have been used to validate the efficacy of hyaluronic acid (HA)-coated nanoparticulate vaccines against respiratory pathogens.[36] While these organoid models have proven essential for evaluating the safety and targeted delivery of nanoparticulate systems, their future potential lies in increasing physiological complexity. By integrating advanced features such as immune infiltration and vascularization, organoids will further enhance our ability to predict long-term systemic interactions and immunogenicity, ultimately serving as a high-fidelity translational bridge for personalized nanomedicine.

Despite these encouraging results, several limitations warrant further investigation. First, the regulatory roles of the ETS1/MYC axis and the therapeutic efficacy of CA9-targeted delivery were primarily validated in cell line derived and patient organoid derived xenograft models. Future studies employing transgenic mouse models, such as tissue-specific ETS1/MYC knockout, are indispensable to fully elucidate the complex spatiotemporal dynamics of these molecular interactions within the intact tumor microenvironment. Second, before clinical translation, the long-term systemic toxicity and immunogenicity of repeated administrations need to be evaluated in relevant animal models. Although we have demonstrated favorable biosafety profiles through body weight monitoring, histopathological examination of major organs, and biodistribution analysis, we recognize that these blood component analyses would provide critical complementary evidence for assessing systemic toxicity and organ function. Finally, the scalability of the microfluidic assembly process for large-scale clinical manufacturing remains a challenge to be addressed.

Conclusion

In summary, this study identifies the ETS1/MYC regulatory axis as a critical driver of ccRCC progression. By integrating bioinformatics with experimental validation, we developed ETS1@Lip-CAIX, a functionalized liposomal nanoplatform surface-modified with an optimized CA9-targeting peptide (CaIX-P7) for precise siETS1 delivery. Our findings demonstrate that this system achieves efficient tumor-specific internalization and intracellular release, effectively silencing the ETS1/MYC signaling. ETS1@Lip-CAIX exhibited robust anti-tumor efficacy and favorable biocompatibility across multiple preclinical models, including cell lines, patient-derived organoids, and in vivo xenografts. Collectively, this research presents a precise and clinically translational nanomedicine strategy for the targeted treatment of aggressive renal malignancies.

Abbreviations

CA9, carbonic anhydrase IX; ccRCC, clear cell renal cell carcinoma; DLS, dynamic light scattering; EE, encapsulation efficiency; LNPs, liposomal nanoparticles; PBS, phosphate-buffered saline; PCA, principal component analysis; PDB, Protein Data Bank; PDI, polydispersity index; PDO, patient-derived organoid; RT-qPCR, real-time quantitative PCR; scRNA-seq, single-cell RNA sequencing; siRNA, small interfering RNA; SPR, surface plasmon resonance; TCGA, The Cancer Genome Atlas; TF, transcription factor.

Data Sharing Statement

These data of this paper can be available from the corresponding authors on reasonable request.

Ethics Approval and Consent to Participate

The study involving human clinical samples was approved by the Ethics Committee of the Second Hospital of Shandong University (Approval No. KYLL2025605), and written informed consent was obtained from all participating patients. All animal experimental procedures were performed in accordance with the Guide for the Care and Use of Laboratory Animals and were approved by the Ethics Committee of the Second Hospital of Shandong University (Approval No. KYLL2025289). All procedures performed in this study involving human participants were in accordance with the ethical standards of the institutional research committee and with the Declaration of Helsinki.

Author Contributions

All authors made a significant contribution to the work reported, whether that is in the conception, study design, execution, acquisition of data, analysis and interpretation, or in all these areas; took part in drafting, revising or critically reviewing the article; gave final approval of the version to be published; have agreed on the journal to which the article has been submitted; and agree to be accountable for all aspects of the work.

Disclosure

The authors report no conflicts of interest in this work.

References

1. Zhang Y, Tuo Z, Lin Y. et al. NRF1 Induces ApoEhigh Cancer-Associated Fibroblasts to Promote Stemness of Renal Cell Carcinoma. *Cancer Res*. 2026;2026:1. doi:10.1158/0008-5472.CAN-25-0959
2. Alves Costa Silva C, Machaalani M, Saliby RM, et al. Soluble MAdCAM-1 as a biomarker in metastatic renal cell carcinoma. *Nat Med*. 2026;32(2):671–681. doi:10.1038/s41591-025-04067-x
3. Ding D, Feng J, Yin G, et al. Synthesis and Preclinical Evaluation of 99mTc-Labeled Benzenesulfonamides for SPECT Imaging of Carbonic Anhydrase IX Expression. *J Med Chem*. 2026;69(1):669–682. doi:10.1021/acs.jmedchem.5c03078
4. Kleinendorst SC, Oosterwijk E, Molkenboer-Kuenen J, et al. Towards effective CAIX-targeted radionuclide and checkpoint inhibition combination therapy for advanced clear cell renal cell carcinoma. *Theranostics*. 2024;14(9):3693–3707. doi:10.7150/thno.96944
5. Martinez-Marin D, Sharma M, Van wunnik JC, et al. Dishevelled-1 regulates global transcriptomic changes and associates with ETS1 transcription factor. *Nat Commun*. 2025;16(1):6288. doi:10.1038/s41467-025-61551-1
6. Antoniolli M, Solovey M, Hildebrand JA, et al. ARID1A mutations protect follicular lymphoma from FAS-dependent immune surveillance by reducing RUNX3/ETS1-driven FAS-expression. *Cell Death Differ*. 2025;32(5):899–910. doi:10.1038/s41418-025-01445-3
7. Qian K, Li W, Ren S, et al. HDAC8 Enhances the Function of HIF-2α by Deacetylating ETS1 to Decrease the Sensitivity of TKIs in ccRCC. *Adv Sci*. 2024;11(36):e2401142. doi:10.1002/advs.202401142
8. VanKeulen-Miller R, Aponte A, Tiwade PB, et al. Characterizing the Impact of the Cell Cycle on mRNA Lipid Nanoparticles. *J Am Chem Soc*. 2026;148(2):2779–2791. doi:10.1021/jacs.5c20083
9. Hu M, Li Y, Cai Y, et al. A Versatile Self-Amplifying mRNA System Consolidates Oncolytic Virus Benefits into a Single Flexible Backbone for Cancer Therapy. *Mol Ther*. 2026;3:S1525. doi:10.1016/j.ymthe.2025.12.066
10. Wang R, Yu J, Caligiuri MA, Ma S. Optimizing In Vivo CAR-T Cell Engineering for Cancer Immunotherapy. *Cancer Res*. 2026;2026:3. doi:10.1158/0008-5472.CAN-25-3748
11. Liao Y, Zeng X, Zhang X, et al. Optimized Lipid Nanoparticles for Co-Delivery of mRNA and siRNA Therapeutics in Refractory Liver Cancer. *Adv Mater*. 2026;9(11):e19473. doi:10.1002/adma.202519473
12. Wang R, Zhang Y, Du S, Li Y, Ren Y, Lin J. Nanoformulations Downregulating METTL16 Combined with mRNA Tumor Vaccines Suppress Triple-Negative Breast Cancer and Prevent Metastasis. *Int J Nanomed*. 2025;20:8951–8966. doi:10.2147/IJN.S520329
13. Askoxylakis V, Ehemann V, Rana S, et al. Binding of the phage display derived peptide CaIX-P1 on human colorectal carcinoma cells correlates with the expression of carbonic anhydrase IX. *Int J Mol Sci*. 2012;13(10):13030–13048. doi:10.3390/ijms131013030
14. Hu A, Yang C, Wang Z, et al. Dual targeting of AMRC12 and Malassezia globosa disrupts MYC liquid condensates-driven nuclear pore complex biogenesis in neuroblastoma. *Theranostics*. 2026;16(6):2866–2886. doi:10.7150/thno.120935
15. Kral AJ, Jia L, Sim G, Wan L, Ishigami Y, Krainer AR. Splice-switching ASOs targeting the AURKA 5' UTR collapse an SRSF1-AURKA-MYC oncogenic circuit in pancreatic cancer. *Mol Cell*. 2026;86(1):60–77.e7. doi:10.1016/j.molcel.2025.12.004
16. Tanimoto A, Ramkumar K, Stewart CA, et al. The impact of targeting TRAF2 and NCK-interacting protein kinase (TNIK) on anti-tumor effect and tumor immune environment in c-MYC-high small cell lung cancer. *J Thorac Oncol*. 2025;21(5):S1556. doi:10.1016/j.jtho.2025.12.102
17. Abu-Remaileh M, Stransky LA, Bhalerao N, et al. Targeting of HIF2-driven cachexia in kidney cancer. *Nat Med*. 2025. doi:10.1038/s41591-025-04054-2
18. Chen JH, Li JJ, Yuan Y, et al. ETS1 and RBPJ transcriptionally regulate METTL14 to suppress TGF-β1-induced epithelial-mesenchymal transition in human bronchial epithelial cells. *Biochim Biophys Acta Mol Basis Dis*. 2024;1870(7):167349. doi:10.1016/j.bbadis.2024.167349
19. Martinez-Serrano CA, Cambra JM, Alvarez-Rodriguez M, et al. Gene dysregulation impairs placental angiogenesis in allogeneic pig pregnancies. *Anim Reprod Sci*. 2025;281:107988. doi:10.1016/j.anireprosci.2025
20. Qiao Q, Guo L, Ma Z. ETS1 facilitates the progression of OSCC and contributes to macrophage M2 polarization via regulating NXPH4. *Cytotechnology*. 2026;78(1):7. doi:10.1007/s10616-025-00869-6
21. Dhara A, Aier I, Das S, et al. Enhanced ETS1 stability by DNAPKcs orchestrates transcriptional changes during chemoresistance in triple negative breast cancer. *NPJ Breast Cancer*. 2025;11(1):114. doi:10.1038/s41523-025-00782-3

22. Xiao L, Zhang Z, Li T, et al. ETS1-Driven Nucleolar Stress Orchestrates OLR1 + Macrophage Crosstalk to Sustain Immunosuppressive Microenvironment in Clear Cell Renal Cell Carcinoma. *Hum Mutat*. 2025;2025(1):8856239. doi:10.1155/humu/8856239
23. Müller M, Georgiev T, Mock J, Neri D, Cazzamalli S, Oehler S. Small Organic Carbonic Anhydrase IX Ligands from DNA-Encoded Chemical Libraries for Tumor-Targeted Delivery of Radionuclides. *J Am Chem Soc*. 2025;147(21):18230–18239. doi:10.1021/jacs.5c05198
24. Fukushima H, Takao S, Furusawa A, et al. Carbonic anhydrase-9-targeted near-infrared photoimmunotherapy as a theranostic modality for clear cell renal cell carcinoma. *Int, J, Cancer*. 2025;156(12):2377–2388. doi:10.1002/ijc.35364
25. Alsaab HO, Sau S, Alzhrani RM, et al. Tumor hypoxia directed multimodal nanotherapy for overcoming drug resistance in renal cell carcinoma and reprogramming macrophages. *Biomaterials*. 2018;183:280–294. doi:10.1016/j.biomaterials.2018.08.053
26. Deng Q, Hua A, Zhao Q, et al. Modulating tumor acidity with hydroxyethyl starch-based nanoparticles by targeting CA9 to eliminate cancer stem cells and overcome immunosuppression. *Biomaterials*. 2026;324:123501. doi:10.1016/j.biomaterials.2025.123501
27. Abosalim HM, El-Moselhy TF, Sharafeldin N, et al. Innovative design and synthesis of dual-acting hCA IX/CDK-2 inhibitors through hetero ring fused pyrimidine utilization for cutting-edge anticancer therapy: zein nanoparticles for in vivo lung cancer treatment. *Bioorg Chem*. 2025;166:109057. doi:10.1016/j.bioorg.2025.109057
28. Yan Y, Lu A, Dou Y, et al. Nanomedicines Reprogram Synovial Macrophages by Scavenging Nitric Oxide and Silencing CA9 in Progressive Osteoarthritis. *Adv Sci*. 2023;10(11):e2207490. doi:10.1002/advs.202207490
29. Tatiparti K, Rauf MA, Sau S, Iyer AK. Carbonic Anhydrase-IX Guided Albumin Nanoparticles for Hypoxia-mediated Triple-Negative Breast Cancer Cell Killing and Imaging of Patient-derived Tumor. *Molecules*. 2020;25(10):2362. doi:10.3390/molecules25102362
30. Pieraccioli M, Ciucci A, Corti C, et al. Single-cell transcriptome analysis of patient-derived organoids captures inter- and intratumor heterogeneity and uncovers targetable pathways in high grade serous ovarian cancer. *Drug Resist Updat*. 2026;85:101354. doi:10.1016/j.drup.2026.101354
31. Shi J, Wu L, Li P, et al. Volumetric compression regulates the phase separation of AXIN and acts as an operational amplifier to bidirectionally modulate Wnt signaling in organoids. *Nat Commun*. 2026;2026:2. doi:10.1038/s41467-025-68209-y
32. Zheng S, Zhang X, Pang Z, Liu J, Liu S, Sheng R. Anti-Pan-Rspo Chimeric Protein-Conjugated Albumin Nanoparticle Provides Promising Opportunities in Cancer Targeted Therapy. *Adv Healthc Mater*. 2023;12(29):e2301441. doi:10.1002/adhm.202301441
33. Zheng S, Guo Y, Han Q, et al. STING agonists and PI3Kγ inhibitor co-loaded ferric ion-punicalagin networks for comprehensive cancer therapy. *Int J Biol Macromol*. 2024;282(Pt 2):136776. doi:10.1016/j.ijbiomac.2024.136776
34. Wang Y, Diao P, Lv P, et al. A human patient-derived organoid biobank to model tumor heterogeneity and therapeutic vulnerability for oral squamous cell carcinoma. *Cell Rep Med*. 2026;7(2):102622. doi:10.1016/j.xcrm.2026.102622
35. Grumelot S, Mannering F, Campbell N, et al. Investigating Nanoparticle Distribution and Tissue Architecture in Male and Female Human Cardiac Organoids. *Chem Eng J*. 2026;529:172977. doi:10.1016/j.cej.2026.172977
36. Zhang Z, Chen H, Xu B, et al. Mucosal-Penetrating Nanovaccine Enhances Mucosal and Systemic Immunity against Respiratory Syncytial Virus Infection. *ACS Nano*. 2026;20(11):9237–9249. doi:10.1021/acsnano.5c19489
37. Wang S, Wang Z, Wu C, et al. Amelioration of colorectal cancer-associated fibroblasts in immunosuppressive microenvironment by ferroptosis-based nanotherapy. *Nat Commun*. 2026;17(1):2778. doi:10.1038/s41467-026-69462-5
38. Luo S, Feng L, Tian B, et al. 3D printed HAMA/GelMA/lignosulfonate hydrogel integrating oxygen-releasing and antioxidative modules for liver regeneration. *J Nanobiotechnology*. 2026;24(1):313. doi:10.1186/s12951-026-04197-5